NASA CR-111950

A STUDY OF THE NEAR FIELDS OF REFLECTOR ANTENNAS USING THE GEOMETRICAL THEORY OF DIFFRACTION

William Charles Roberts-Horsfield, III

The Ohio State University

ElectroScience Laboratory

Department of Electrical Engineering
Columbus, Ohio 43212

Contract No. NAS1-10040

August 1971

NASA, Langley Research Center
Langley Station
Hampton, Virginia 23365

NASA CR-111950

A STUDY OF THE NEAR FIELDS OF REFLECTOR ANTENNAS USING THE GEOMETRICAL THEORY OF DIFFRACTION

By William Charles Roberts-Horsfield, III

Prepared under Contract No. NAS1-10040 by
THE OHIO STATE UNIVERSITY ELECTROSCIENCE LABORATORY
Department of Electrical Engineering
Columbus, Ohio 43212

for

NATIONAL AERONAUTICS AND SPACE ADMINISTRATION

ABSTRACT

A technique for calculating the near fields of reflector antennas using the geometrical theory of diffraction is developed. Computed patterns for two antennas are compared with patterns obtained by other techniques and experimental data. The GTD is proved to be a useful tool in obtaining near field patterns of antennas.

CONTENTS

I. Introduction

The study of the near fields of antennas has several practical applications. Siting high power radars demands a knowledge of the near field pattern of the system so that hazards to personnel and flammable or explosive material may be calculated and satisfactory safety margins established. Since a radome is, almost exclusively, located in the near field of the antenna it houses, its effect on the pointing accuracy and beam shape of the antenna depends on the near field distribution at the surface of the radome. Thus a design minimizing pointing errors and pattern degradation must be based on a knowledge of the near fields of the antenna. With the advent of millimeter wave experiments (16 GHz - 90 GHz) the near field of an antenna may extend a large distance from the antenna. For example, the Fresnel zone of a thirty-foot diameter antenna operating at 32 GHz extends to 58,000 feet as obtained from the far field condition $\frac{2D^2}{\lambda}$. Thus atmospheric disturbances affect ground to satellite communication entirely through interaction with the near field of the antenna. The simplifying approximations to the radiation integrals which enable simple calculation of the far field patterns of large antennas are not applicable in the near field. Solution of the exact radiation integrals in the near field requires a sizeable investment of computation time and machinery for all but the smallest antennas. The computation time and the size of the machine required increases sharply with the

size of the antenna. The geometrical theory of diffraction provides an attractive alternative to the classical theory for the solution of near field problems. The techniques used in this study reduce the area integration required in the exact method to, at worst, a line integration and, at best a summation of a few discrete terms.

The problem is restricted here to the determination of the forward near fields of reflector antennas in a cylindrical region with diameter twice the antenna diameter using the geometrical theory of diffraction. This region is treated since it represents the portion of the task that is not clearly included in previous solutions. The geometrical theory of diffraction is a logical extension of the theory of geometrical optics; it introduces a class of rays generated by the interaction of the incident field with a discontinuity of the boundary (in our case a sharp edge.) An intuitive analysis of the effects of the edge shows that the diffraction products act to remove the discontinuity in the fields at the boundary between the illuminated, and shadowed, regions of both the incident and reflected fields. This theory has been applied to the study of two-dimensional aperture antennas by Clark for near zone scattering.[1] Lysher used Babinet's principal to obtain the near zone fields in the rear hemisphere of a reflector antenna by analyzing the fields of an aperture.[2] In the aperture model, a plane wave, or in Lysher's case, a spherical wave, illuminates an opaque screen with an aperture.

The antenna beam is represented by the portion of the wave passing through the aperture. Clearly, this model only represents one shadow boundary properly. Reflector antennas use a shaped reflector to focus the diverging rearward directed field of a feed into a collimated forward directed beam.[3] Two shadow boundaries are associated with this geometry, one the incident shadow boundary caused by the reflector shadowing the feed field, and the second, or reflection, shadow boundary between the reflected, focused, beam and the surrounding shadow. Note that the incident shadow boundary is improperly positioned in aperture models of reflector antennas. Ratnasiri, Kouyoumjian and Pathak have applied the geometrical theory of diffraction to the study of the wide angle side lobes of reflector antennas in the far field.[4]

II. The Near Fields of Three-Dimensional Reflector Antennas

The analysis of a three-dimensional problem by the geometrical theory of diffraction is an extension of two-dimensional diffraction theory. The third dimension of the problem is introduced using either of two methods. First, if the field point is not near a caustic, the concepts of edge diffraction may be used. If the field point is near a caustic, the usual edge diffraction concept may be extended by use of an equivalent current technique. If the geometry involves a shadow boundary near the caustic, the equivalent current method yields the correct result only in the near half of the Fresnel zone.

The general method used in this paper is to model the radiated field of the antenna by the geometrical optics field and the diffraction fields associated with the shadow boundaries of the geometrical optics field. The diffraction fields of the antenna will be calculated from the position of the shadow boundaries, and these fields will be summed with the geometrical optics fields to obtain the total Fresnel zone fields.

A. Basic Concepts

1. Review of Half-Plane Diffraction Mechanisms

Figure 1 illustrates the various diffraction regions when a point source illuminates a semi-infinite, planar, opaque, reflecting screen. For the point P in region I, the field at P is composed of a direct ray from S and a ray reflected from the plane. In going from region I to region II, the reflection shadow boundary is crossed and now only the direct ray illuminates P. Finally going to region III, we cross the incident

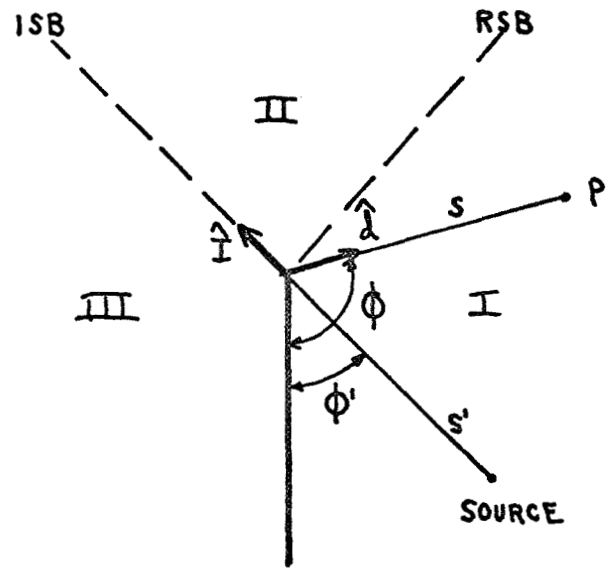

Figure 1: Point Source Illuminating a Half Plane

shadow boundary; and P is in the geometrical optics shadow of the half plane. In addition to the geometrical optics rays, there exist a class of rays caused by edge scattering.

Sommerfeld[5] first solved the scattering or diffraction problem for a source distance of infinity or plane wave incidence. Pathak and Kouyoumjian[6] recently obtained an asymptotic solution for a finite source distance. The special case of their solution for illumination normal to the edge will be used in the present analysis.

If $u^i(s', \phi')$ is the field of the incident scalar wave at the edge, the diffracted fields are given by

$$u^d_{s_H}(s,\phi) = u^i(s',\phi') D_{s_H}(\phi,\phi') \sqrt{\frac{s'}{s(s+s')}}\; e^{-jks}, \tag{1}$$

where the scalar diffraction coefficients are

$$D_{s_H}(\phi,\phi') = -\frac{e^{-j\frac{\pi}{4}}}{2\sqrt{2\pi k}}\left[\frac{F(kLa_-)}{\cos\frac{\phi-\phi'}{2}} \mp \frac{F(kLa_+)}{\cos\frac{\phi+\phi'}{2}}\right]\frac{1}{\sin\beta}, \tag{2}$$

$$F(kLa_\pm) = j2\sqrt{kLa_\pm}\, e^{jkLa_\pm}\int_{\sqrt{kLa_\pm}}^{\infty} e^{-j\tau^2}\, d\tau, \tag{3}$$

$$a_\pm = 2\cos^2\frac{\phi \pm \phi'}{2}, \tag{4}$$

$$L = \frac{ss'}{s+s'}\sin^2\beta, \tag{5}$$

and ϕ, ϕ', S, and S' are shown in Figure 1. $F(kLa\pm)$ is a correction factor that is needed only near the respective shadow boundary. When $kLa^\pm > 10$, $F(kLa^+)$ can be replaced by unity.

The following coordinate transformations make the notation more compact and reinforce the concept that the diffraction fields are intimately related to the location of the shadow boundaries. The first term in (2) can be associated with the incident shadow boundary and the second with the reflection shadow boundary. We can relate these terms to the angular

distance from the shadow boundary.

$$\phi - \phi' = \theta^i + \pi \tag{6}$$

$$\phi + \phi' = \theta^R + \pi \tag{7}$$

Where θ^i, θ^R are the angles from the field point to the incident and reflection shadow boundary, respectively, θ is positive in the shadow region. The diffraction coefficient is separated into the incident and reflected components, which may be expressed as

$$D_{S,H}^{i,R}(\theta^{i,R}) = \frac{e^{-j\pi/4}}{2\sqrt{2\pi k}} \frac{F(kLa_{S,H}^{i,R})}{\sin\frac{\theta^{i,R}}{2}}, \tag{8}$$

where

$$a_{S,H}^{i,R} = 2\sin^2\frac{\theta^{i,R}}{2}. \tag{9}$$

From (2) and (8) we see

$$D_{S,H}(\phi,\phi') = D^i(\theta^i) + D^R(\theta^R). \tag{10}$$

Kouyoumjian and Pathak have constructed a simple dyadic diffraction coefficient for vector fields using the soft and hard boundary scalar diffraction coefficients.

$$\bar{\bar{D}}(\phi,\phi') = \hat{e}\hat{e}\, D_S(\phi,\phi') + \hat{\beta}_0\hat{\beta}_0\, D_H(\phi,\phi'), \tag{11}$$

where

$\hat{e}$ is the unit vector tangent to the edge,

$\hat{p} = \hat{e} \times \hat{I}$ where $\hat{I}$ is the unit vector in the direction of incidence, and

$\hat{pd} = \hat{e} \times \hat{d}$ where d is the unit vector in the direction of diffraction.

Using the dyadic diffraction coefficient, one finds

$$\tilde{E}^d(s,\phi) = \bar{\bar{D}}(\phi,\phi') \cdot E^i(s',\phi') \sqrt{\frac{s'}{s(s+s')}}\ e^{-jks}. \tag{12}$$

To find the diffraction fields of a parabolic reflector, the above results must be extended to include the effect of a curved screen with a curved edge.

2. Effect of Surface Curvature

The diffraction fields act to eliminate the discontinuity at the shadow boundary. On the shadow boundary sufficiently removed from the edge, the diffracted field is exactly half the difference between the geometrical optics fields on the illuminated and shadow sides of the boundary. The diffracted fields at the shadow boundary of a half plane illuminated by a point source are given by (12) and the incident geometric fields on the shadow boundary by

$$E^{g.o.}(s,\phi'+\pi) = E^i(s',\phi')\ \frac{s'}{s+s'}. \tag{13}$$

Since on the shadow boundary sufficiently removed from the edge

$$\left|E^d(s,\phi'+\pi)\right| = \left|\frac{\tilde{E}^{g.o.}(s',\phi'+\pi)}{2}\right|, \tag{14}$$

then

$$D(\phi'+\pi,\phi') = \frac{1}{2}\sqrt{\frac{ss'}{s+s'}} = \frac{\sqrt{L}}{2}. \qquad (15)$$

The last term in (15) is obtained by solving (8) for a = 0. L is forced to depend on the source and observation distances to properly match the decay of the diffracted wave with distance to the decay of the geometrical optics wave.

The key point is that L is determined by the divergence of the geometrical optics component. The divergence of the geometrical optics component at the incident shadow boundary is determined solely by the actual source and observation point distances. The divergence of the reflected field, however, depends on the curvature of the reflecting surface as well as the source and observation point distances. This effect of surface curvature can be included by determining the location of the image of the source and computing the divergence of the reflected ray using the image distance. Since the parameter L depends on the divergence of the associated geometrical optics field, L also depends on the image distance. Thus L will be different for the incident and reflection diffraction coefficients if the screen is curved. For the parabolic dish with the feed at the focus, s' for the reflection diffraction coefficient will be infinity because the reflected geometrical optics field is that of a plane wave.

3. Effect of Edge Curvature

One of the basic concepts in geometrical optics is the

power conservation in a tube of rays. The assertion is since power flows only along rays and not transverse to them, the power flux in a region bounded by rays is a constant. Thus the power and the fields at two points can be related to the cross section of the ray tube at these points.

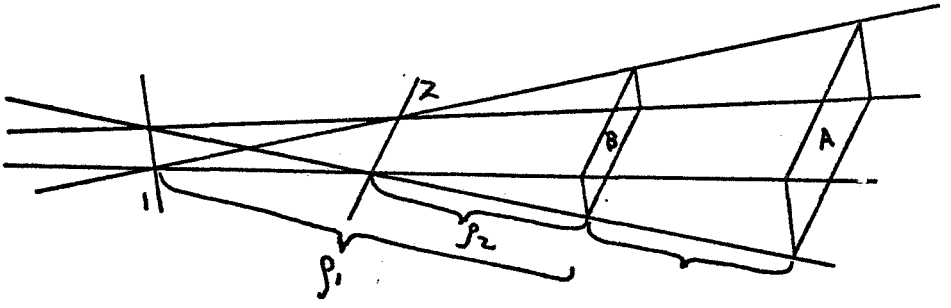

Figure 2: Astigmatic Ray Tube

Given the astigmatic ray tube shown in Figure 2 the ratios of the areas of the surfaces A, B may be expressed

$$\frac{A}{B} = \frac{(\rho_1+r)(\rho_2+r)}{\rho_1 \rho_2}, \tag{16}$$

Since the power flux is constant, the power density is inversely proportional to the area, and the field intensity is inversely proportional to the square root of the area.

$$U_a = U_b \sqrt{\frac{\rho_1 \rho_2}{(\rho_1+r)(\rho_2+r)}} \tag{17}$$

Lines 1 and 2 in Figure 2 are referred to as caustics of the ray

tube, and ρ_1, ρ_2 are their associated caustic distances.

In the diffraction problem the diffracting edge is one caustic of the ray tube. The other caustic is determined by the geometry of the edge. A new formula for the second caustic distance has been developed using differential geometry.[7]

$$\frac{1}{\rho} = \frac{1}{\ell} - \frac{\hat{n}\cdot(\hat{I}-\hat{d})}{\rho_e \sin^2\beta}, \tag{18}$$

where

ρ is the caustic distance,

l is the distance from the diffracting point on the edge to the source,

ρ_e is the radius of curvature of the edge,

$\hat{n}$, $\hat{e}$ are the unit vectors normal and tangent to the edge,

$\hat{I}$, $\hat{d}$ are unit vectors in the direction of the incident and diffracted rays, and

β is the angle between $\hat{I}$ and $\hat{e}$.

Applying (18) to a disc with source on the axis, one finds that the position of the caustic of the diffracted rays is the disc axis.

Since the geometry is symmetrical about the z axis, one can choose any plane through the z axis. When the field point P is in the yz plane,

$$\hat{n} = \hat{y}, \tag{19}$$

$$\hat{I} = \hat{y}\frac{A}{\ell} - \hat{z}\frac{b}{\ell}, \quad \text{and} \tag{20}$$

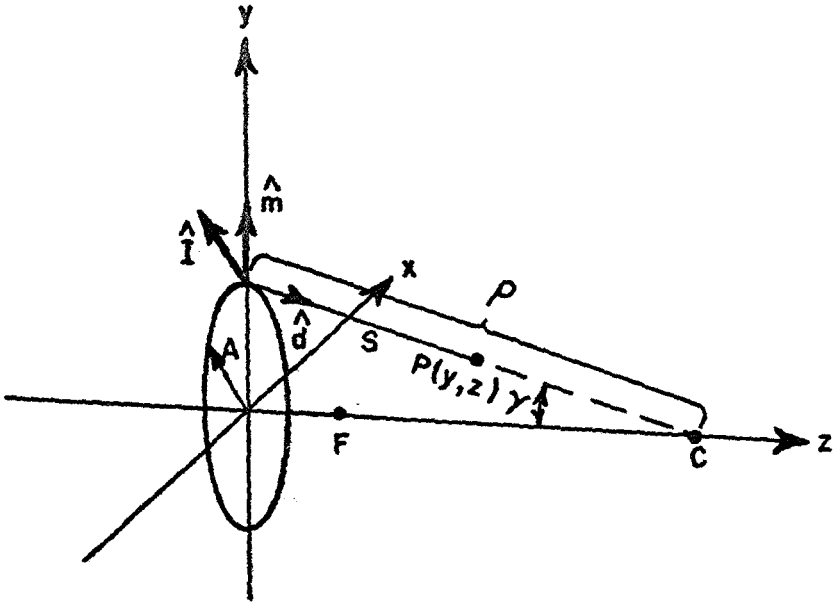

Figure 3: Geometry Used to Find Caustic Distance

$$\hat{\ell} = -\hat{y}\sin\gamma + \hat{z}\cos\gamma, \tag{21}$$

where

y,z are the coordinates of the field point,

A is the radius of the disc,

b is the normal distance from the disc to the source, and

γ is the angle between $\hat{d}$ and the z axis.

From (18) the caustic distance ρ, shown in Fig. 3 is

$$\frac{1}{\rho} = \frac{1}{\ell} - \frac{\hat{y}\cdot\left(\hat{y}\frac{A}{\ell} - \hat{z}\frac{b}{\ell} + \hat{y}\sin\gamma - \hat{z}\cos\gamma\right)}{A}, \tag{22}$$

$$\frac{1}{\rho} = \frac{1}{\ell} - \frac{1}{\ell} + \frac{\sin\gamma}{A}, \tag{23}$$

or

$$\rho = \frac{A}{\sin\gamma}. \tag{24}$$

Thus ρ is the distance on a line passing through the edge, P, and the z axis, from the edge to the z axis.

From similar triangles,

$$\left|\frac{\rho}{\rho+s}\right| = \left|\frac{A}{\gamma}\right|. \tag{25}$$

In this equation ρ is negative if the caustic and P lie on the same side of the edge. Substituting this result into (1) with $S' = \rho$, we obtain

$$\bar{E}^d(s,\phi) = \bar{E}^i(s',\phi')\cdot\bar{\bar{D}}(\phi,\phi')\sqrt{\frac{A}{sy}}\; e^{-jks}\left[e^{j\frac{\pi}{2}}\right]. \tag{26}$$

The term in the brackets provides for the $\frac{\pi}{2}$ phase jump encountered on passing through the caustic. It is included only if the caustic lies between the edge and P.

B. E-Plane Analysis

1. Review of the Two-Point Technique

Keller[8] developed an extension to Fermat's principle which relates the angle of diffraction to the angle of incidence. This extension states that a ray striking an edge excites a family of diffracted rays which form a cone of half angle equal to the angle between the incident ray and the edge. Thus, for all field points not on a caustic of the edge, one can construct a finite number of edge diffracted rays which reach that field point. For the straight edge, only one ray fits this condition, while for the circular disc two rays are sufficient to describe the diffraction effects.

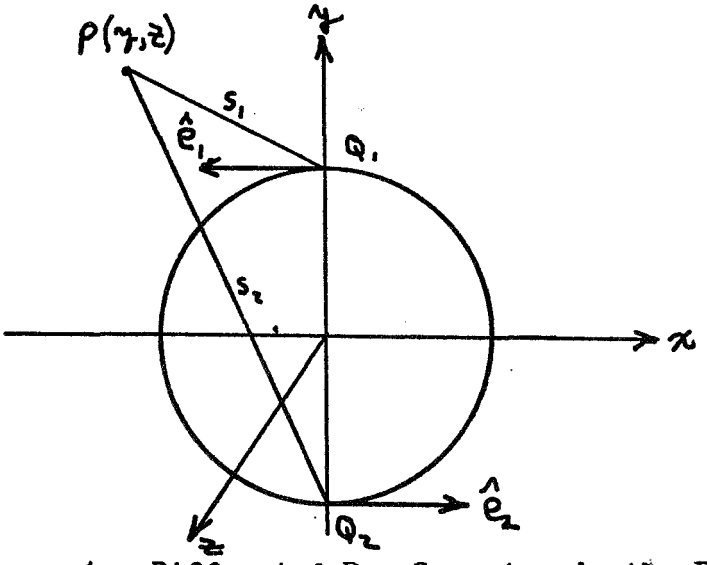

Figure 4: Diffracted Ray Geometry in the E-Plane (Front View)

The fields will be calculated in the region $y > 0$, $z > 0$. Pattern symmetry allows these results to be reflected in the z axis to obtain the complete pattern. In the E-plane from Figure 4, the two points Q_1, Q_2 lie on the y axis and $\hat{e}_1$, $\hat{e}_2$ are $+\hat{x}$, $-\hat{x}$ respectively. The field point is at y, z; the subscript n identifies the diffracting point; and the superscripts i, r associate the term with the incident or reflection shadow boundary. Since Θ is positive in the shadow region, and E^i is contained in the yz plane, equation (25) reduces to

$$\bar{E}^d(s,\phi) = -(-1)^m \hat{\theta}_m E^i(Q_m) D_h(\phi,\phi') \sqrt{\frac{A}{\gamma s_m}}\, e^{-jks_m}\, e^{j(m-1)\pi/2} . \tag{27}$$

Using (10) to resolve D_h into its components and (6) and (7) to relate ϕ, ϕ', Θ^i and Θ^r we find

$$\bar{E}^d(y,z) = (-1)^m \hat{\theta}_m E^i(Q_m)\left[D^i(\theta_m^i) + D^r(\theta_m^r)\right] X \sqrt{\frac{A}{\gamma s_m}}\, e^{-jks_m}\, e^{j(m-1)\pi/2}, \tag{28}$$

where $s_n, \theta_n^r, \theta_n^i$ are obtained from the coordinates of the field point using the following transformation and Figure 5

$$\theta_m^r = -\mathrm{ARCTAN}\,\frac{A + (-1)^m y}{z} \tag{29}$$

$$\theta_m^i = \theta_m^r - \pi + \alpha \tag{30}$$

The sign of Θ must be carefully preserved.

$$s_m = \frac{z}{\cos\theta_m^r} \tag{31}$$

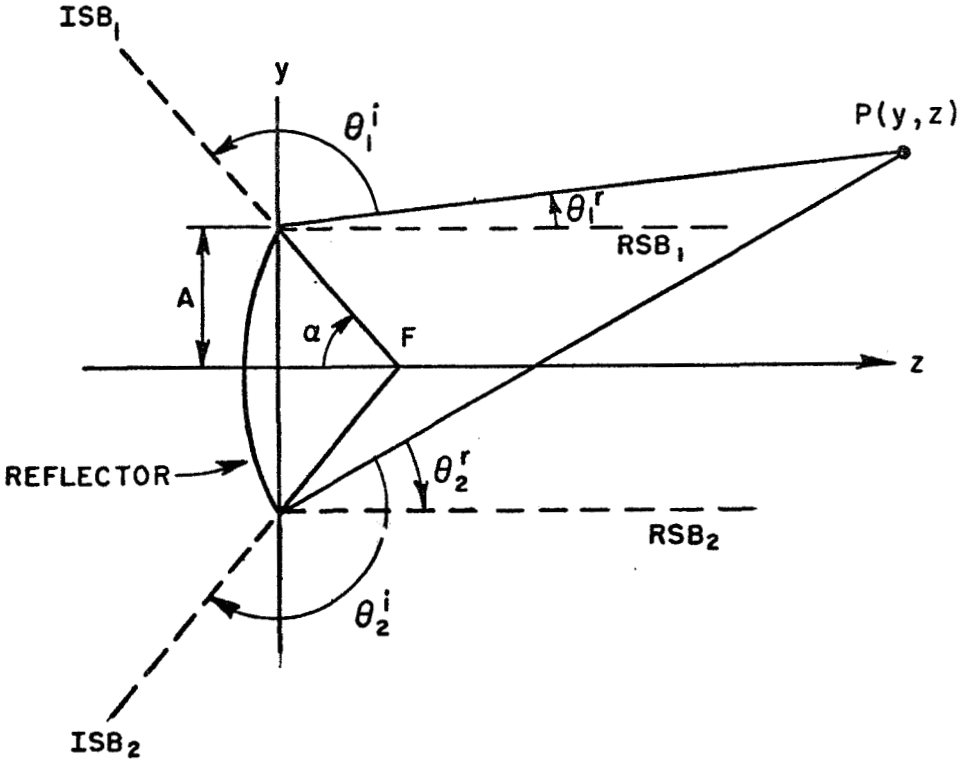

Figure 5: Geometry of Two-Point E-Plane Analysis

α is shown in Figure 5

Resolving $\bar{E}^d$ into axial and transverse components

$$\hat{\theta}_m = -(-1)^m \hat{y} \cos\theta_m - \hat{z} \sin\theta_m . \tag{32}$$

Thus

$$E_z^d(Y,z) = -\sum_{m=1}^{2} (-1)^m E^i(Q_m)\left[D^i(\theta_m^i) + D^{\sim}(\theta_m^{\sim})\right]\sqrt{\frac{A}{Ys_m}}\, X$$

$$X e^{-jks_m} e^{j(m-1)\frac{\pi}{2}} \sin(\theta_m^{\sim}), \tag{33}$$

and

$$E_y^d(Y,z) = -\sum_{m=1}^{2} E^i(Q_m)\left[D^i(\theta_m^i) + D^{\sim}(\theta_m^{\sim})\right]\sqrt{\frac{A}{Ys_m}}\, X$$

$$X e^{-jks_m} e^{j(m-1)\frac{\pi}{2}} \cos(\theta_m^{\sim}), \tag{34}$$

2. Review of the Equivalent Current Technique

When the field point is on or near the axis (corresponding to a caustic) the two-point method fails. For points in the vicinity of the axis, a method based on equivalent current flowing on the rim of the dish is available.

The diffraction field of a half plane may be represented by equivalent currents flowing on the edge of the plane. To derive these currents consider the diffraction field when the electric field is parallel to the edge

$$\bar{E}^d(P) = \bar{E}^i(Q) D_s(Q) \frac{e^{-jks}}{\sqrt{s}}, \tag{35}$$

and when the magnetic field is parallel to the edge,

$$\bar{H}^d(P) = \bar{H}^i(Q)\, D_H(Q)\, \frac{e^{-jks}}{\sqrt{s}} . \tag{36}$$

These fields can be considered to be due to currents of electricity and magnetism flowing along the edge.

$$E^d(P) = -kz_0 \frac{e^{j\frac{\pi}{4}}}{\sqrt{8\pi ks}}\, I \tag{37}$$

$$H^d(P) = -ky_0 \frac{e^{j\frac{\pi}{4}}}{\sqrt{8\pi ks}}\, m \tag{38}$$

In the general case one must take the component of the field tangent to the edge, then equating (35) with (37) and (36) with (38)

$$I = -\frac{\hat{e}\cdot\bar{E}^i(Q)}{z_0}\, D_s(Q)\sqrt{\frac{8\pi}{k}}\, e^{-j\frac{\pi}{4}} , \tag{39}$$

$$m = -\hat{e}\times\hat{I}\cdot\bar{E}^i(Q)\, D_H(Q)\sqrt{\frac{8\pi}{k}}\, e^{-j\frac{\pi}{4}} . \tag{40}$$

A standard radiation integral can now be used to find the fields due to these currents.

In the present problem these currents flow on the edge of a circular disc so that the vector and scalar products in (39) and (40) simplify to trigonometric functions. The field of the feed is assumed to be constant around the edge of the antenna, i.e. the feed E-plane and H-plane patterns are identical.

The electric field due to the electric and magnetic currents

are given by the following integrals:

$$\bar{E}^e = \frac{jkAz_0}{4\pi}\int_0^{2\pi} \frac{e^{-jkr}}{r} I(\phi')\,\hat{r}\times\hat{r}\times\hat{\phi}'\,d\phi', \tag{41}$$

$$\bar{E}^m = \frac{jkA}{4\pi}\int_0^{2\pi} \frac{e^{-jkr}}{r} M(\phi')\,\hat{r}\times\hat{\phi}'\,d\phi'. \tag{42}$$

The above integrals assume that the field point is in the far field of the incremental sources even though it is in the near field of the totality of sources. As long as the incremental source to field point distance is greater than 1.6 wavelengths, this is a valid approximation.[9] Substituting (39) and (40) in (41) and (42) gives

$$\bar{E}^d = \bar{E}^e + \bar{E}^m = \frac{jAe^{-j\frac{\pi}{4}}}{\sqrt{\lambda}}\int_0^{2\pi} E^i(\phi')\,\frac{e^{-jkr}}{r}\times$$

$$\times\left[D_S(\phi')(\hat{r}\times\hat{r}\times\hat{\phi}')\cos\phi' + D_H(\phi')\,\hat{r}\times\hat{\phi}'\sin\phi'\right]d\phi'. \tag{43}$$

On the axis of the antenna the above integral simplifies considerably. The slant range, r, is a constant and the vector products reduce to

$$\hat{r}\times\hat{r}\times\hat{\phi}' = -\hat{\phi}' = \hat{x}\sin\phi' - \hat{y}\cos\phi', \tag{44}$$

$$\hat{r}\times\hat{\phi}' = -\hat{\rho}\frac{z}{r} - \hat{z}\frac{A}{r} = -\hat{x}\frac{z}{r}\cos\phi' - \hat{y}\frac{z}{r}\sin\phi' - \hat{z}\frac{A}{r}, \tag{45}$$

Substituting these results in the radiation integral and performing the integration, one obtains for the axial case

$$\bar{E}^{\ell} = -\hat{y}\, j\frac{A\sqrt{8\pi h}}{4}\,\frac{e^{-j(kr+\pi/4)}}{r}\left[\frac{z}{r}D_h(\theta)-D_s(\theta)\right]. \qquad (46)$$

The fields in the transition zone near the axis where the two-point method gives questionable results may be calculated using an extension of the technique used on the axis. We can compute the fields using the radiation integrals, inserting the actual incremental source to field point distance in the integrals to account for the new location of the field point off the axis.

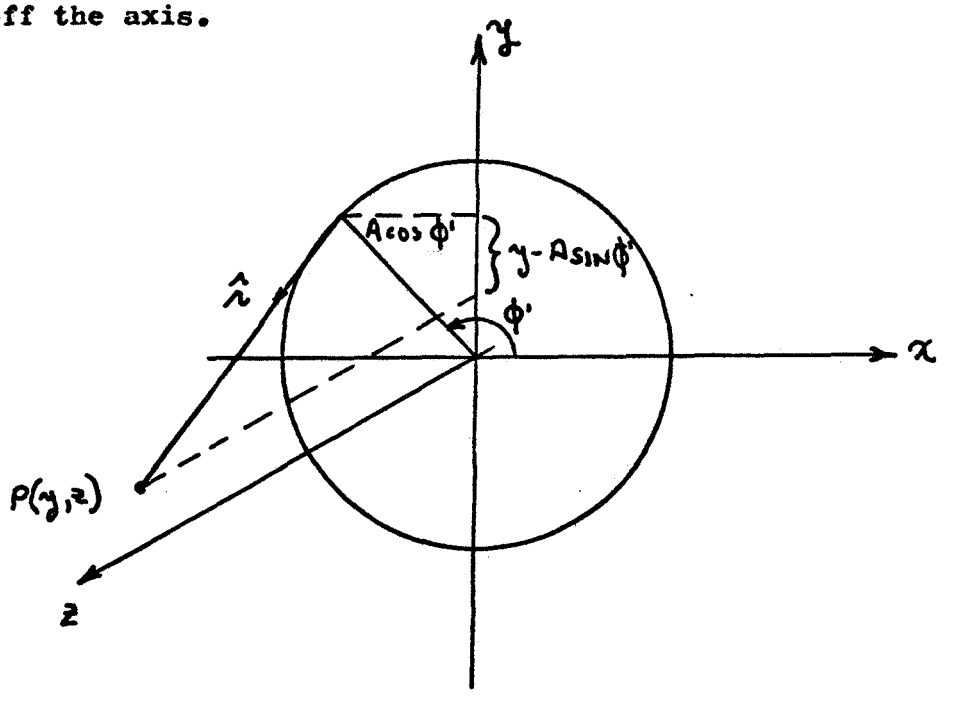

Figure 6: Determination of $\hat{r}$ Near z Axis

From Figure 6 for a pattern in the yz plane

$$r = \sqrt{z^2+(A\cos\phi')^2+(y-A\sin\phi')^2}\,, \qquad (47)$$

$$\hat{\rho} = -\hat{x}\,\frac{A\cos\phi'}{\rho} + \hat{y}\,\frac{(y - A\sin\phi')}{\rho} + \hat{z}\,\frac{z}{\rho}, \tag{48}$$

$$\hat{\phi}' = -\hat{x}\sin\phi' + \hat{y}\cos\phi' . \tag{49}$$

For field points close to the axis $D_{\substack{s\\h}}(Q)$ is relatively constant. We can take $D_{\substack{s\\h}}(Q)$ constant at its value for the on axis case

$$D_{\substack{s\\H}}(Q) = D^{i}(\theta^{i}) \mp D^{\sim}(\theta^{\wedge}), \tag{50}$$

where θ^{i}, $\theta^{\sim}$ are obtained from (30, (31) for y = 0.

The equivalent current method will fail in the far field when a shadow boundary and a caustic of the diffracted rays are parallel.

In the case of back scatter from the two-dimensional strip, one can show that the geometrical theory of diffraction provides proper transition to the far field behavior; and the same is true of a three-dimensional problem with diverging shadow boundaries.

For the strip, consider Figure 7. With the electric field parallel to the strip edge, the diffracted fields are

$$E^{d}_{H} = E^{i}(\infty, \pi/2)\, D_{H}(\phi, \pi/2)\sqrt{\frac{1}{s}}\, e^{-jks}, \tag{51}$$

since $\phi' = \pi/2$, $s' = \infty$ for a plane wave at normal incidence. The reflected fields are

$$E^{g.o.} = -E^{i}(\infty, \pi/2)\, e^{-jks}. \tag{52}$$

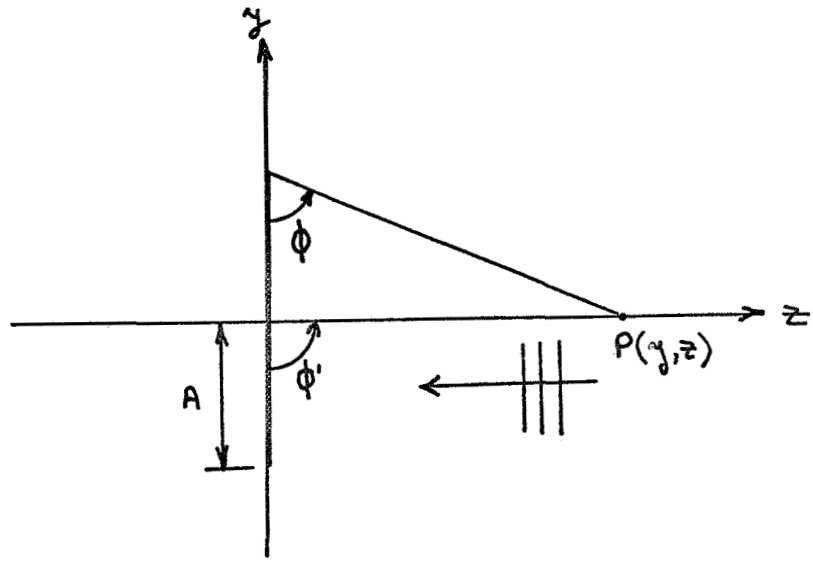

Figure 7: Conducting Strip Illuminated by a Plane Wave

Referring to (2), (3) when $s' = \infty$ and $L = s$

$$D_N(\phi, \pi/2) = -\frac{e^{-\pi/4}}{2\sqrt{2\pi k}}\left[\frac{1}{\cos\frac{\phi-\phi'}{2}} + \right.$$

$$\left. + \frac{j4\sqrt{ksa_+}\, e^{jksa_+}}{\sqrt{a_+}\,\mathrm{sgn}\left(\cos\frac{\phi+\phi'}{2}\right)} \int_{\sqrt{ksa_+}}^{\infty} e^{-j\tau^2}\, d\tau \right]. \qquad (53)$$

As we go to the far field on the axis

$$\lim_{\substack{s\to\infty \\ \phi\to\pi/2}} \sqrt{ksa_+} = \sqrt{\frac{kA^2}{2z}}, \qquad (54)$$

and the second term in D_h predominates

$$E_h^d(s,\phi) = -j E^i \frac{e^{-j\left(\frac{\pi}{4}+ks\right)}}{\sqrt{2\pi}} X$$

$$X \int_{\sqrt{ksa_+}}^{\infty} e^{-j\tau^2} d\tau \; sgn\left(\cos\frac{\phi+\phi'}{2}\right). \tag{55}$$

Now

$$\int_{x}^{\infty} e^{-j\tau^2} d\tau = \frac{\sqrt{\pi}}{2} e^{-j\frac{\pi}{4}} - \int_{0}^{x} e^{-j\tau^2} d\tau . \tag{56}$$

For $\sqrt{\frac{kA^2}{2z}}$ small, the second term in (55) can be represented as

$$\int_{0}^{\sqrt{\frac{kA^2}{2z}}} e^{-j\tau} d\tau \cong \sqrt{\frac{kA^2}{2z}} . \tag{57}$$

$$E_h^d = -E^i \left\{ \frac{e^{-jks}}{2} + j\sqrt{\frac{k}{\pi z}} \frac{A}{2} e^{-j\left(\frac{\pi}{4}+ks\right)} \right\} sgn\left(\cos\frac{\phi+\phi'}{2}\right) \tag{58}$$

When the diffracted fields from the two edges interact with the geometrical optics field, the first term in (58) just cancels the geometrical optics field and we are left with

$$E^T(s) = j E^i \sqrt{\frac{k}{\pi z}} \frac{A}{2} e^{-j\left(\frac{\pi}{4}+ks\right)}, \tag{59}$$

which is the expected result.

Now for the three-dimensional case with diverging shadow boundaries consider Figure 8.

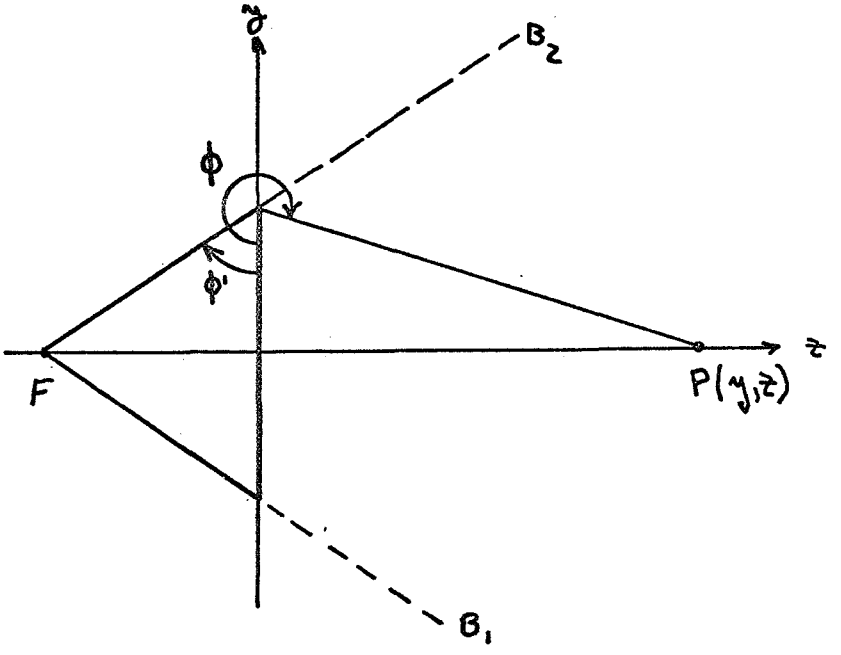

Figure 8: Disc Illuminated by Source at Finite Distance

A source located at F illuminates a disc giving rise to the shadow boundaries, B_1, B_2.

As P recedes to the far field ϕ goes to the limit of $\frac{3\pi}{2}$. Thus eventually kLa will be greater than 10, and the approximate form

$$D(\phi,\phi') = \frac{e^{-j\frac{\pi}{4}}}{2\sqrt{2\pi k}} \frac{1}{\cos\frac{\phi+\phi'}{2}}, \tag{60}$$

may be used.

From (39) and (60)

$$I \cong -\frac{E^i}{z_0} \frac{e^{-j\frac{\pi}{4}}}{2\sqrt{2\pi k}} \sqrt{\frac{8\pi}{k}} \frac{e^{-j\frac{\pi}{4}}}{\cos\frac{\phi+\phi'}{2}} = j\frac{E^i}{z_0 k \cos\frac{\phi+\phi'}{2}}. \tag{61}$$

Inserting (61) into the radiation integral

$$E^e \cong \frac{jkAz_0 e^{-jkz}}{4\pi z} \int_0^{2\pi} \frac{j E^i}{z_0 k \cos\frac{\phi+\phi'}{2}} \cdot \tag{62}$$

Finally

$$E^e \cong -\frac{e^{-jkz}}{4\pi z} \cdot \tag{63}$$

The result is correct to within a constant factor. The correct constant would be obtained if the magnetic current had also been included.

When computing the field near the shadow boundary, the equivalent current concept fails since the diffracted fields do not have the appropriate $\frac{1}{\sqrt{r}}$ dependence for the two-dimensional geometry, and hence these diffracted fields cannot be equated to the fields of an infinite current source.

III. Near Fields of a Uniform Antenna

In this section, the near fields of a uniformly illuminated antenna 10 wavelengths in diameter will be calculated. The near fields will be calculated for both the aperture model and the reflector geometry. Recall that the aperture model considers only the shadow boundary associated with the main beam, while the reflector geometry also includes the effect of the shadow of the reflector in the feed pattern. Direct feed radiation and aperture blockage effects will not be considered.

The equations developed in Section II were programmed in Fortran IV and run on the IBM 360-75 of the IRCC. The electric field was computed for planes 2, 10, 20 and 40 wavelengths in

front of the antenna using the two-point method off the axis and the equivalent current method on the axis. The results are compared with similar data calculated by Wu[10], using plane wave spectrum concept and also aperture integration. Two results are presented for each distance, one including the effects of the incident shadow boundary and one neglecting it.

The agreement between the diffraction theory results and the plane wave spectrum-aperture integration is very good. Resolution of the slight difference between the results would require resorting to more elegant methods of field analysis. The plane wave spectrum and aperture integration techniques both use the physical optics approximations to the actual field in the aperture. The assumption that the field is constant across the aperture neglects the interaction of the aperture edges with the field. An exact analysis using an integral equation or eigenfunction technique would resolve the question.

Figure 9 compares the GTD and aperture integration results at a range of 2 wavelengths from the antenna. The equivalent current technique was used to obtain field values for points out to one wavelength on either side of the axis. At this range, the two-point method and the equivalent current method agreed to within 0.2λ of the axis. In all the figures the erroneous two-point data near the axis is shown by the dotted lines. Figure 10 compares the GTD and aperture

integration results 10 wavelengths from the antenna. Again the equivalent current technique agreed with the two-point method beyond 0.2 λ from the axis. Note that the GTD solution shows that the field on the axis is less at 10 λ than at both 2 λ and 20 λ. Figures 11 and 12 show the GTD results for distances of 20 and 40 wavelengths respectively. At 20 λ the two-point method began to show some error 0.5 λ from the axis and got worse closer to the axial caustic. The error was appreciably greater than in the 2 λ and 10 λ cases. At 40 λ the two-point method began to fail 1 λ from the axial caustic. At this range the two-point method error near the axis was greater than in any of the smaller ranges.

Figure 13 shows the field on the axis as a function of range. The parameter $\overline{X}$ is the ratio of the distance to the far field criterion. Note the oscillatory behavior of the field near the antenna. The field reaches the furthest maximum at 22 wavelengths and then should show $\frac{1}{r}$ decay. The failure of the equivalent current method is clearly seen in this figure. Note the increasing field with distance beyond 160 wavelengths.

Agreement between the GTD and aperture integration results is quite good. Reference to Tables I - IV will reveal that the effect of the incident shadow boundary is strongest at the greatest transverse distances where the reflection shadow boundary term is small.

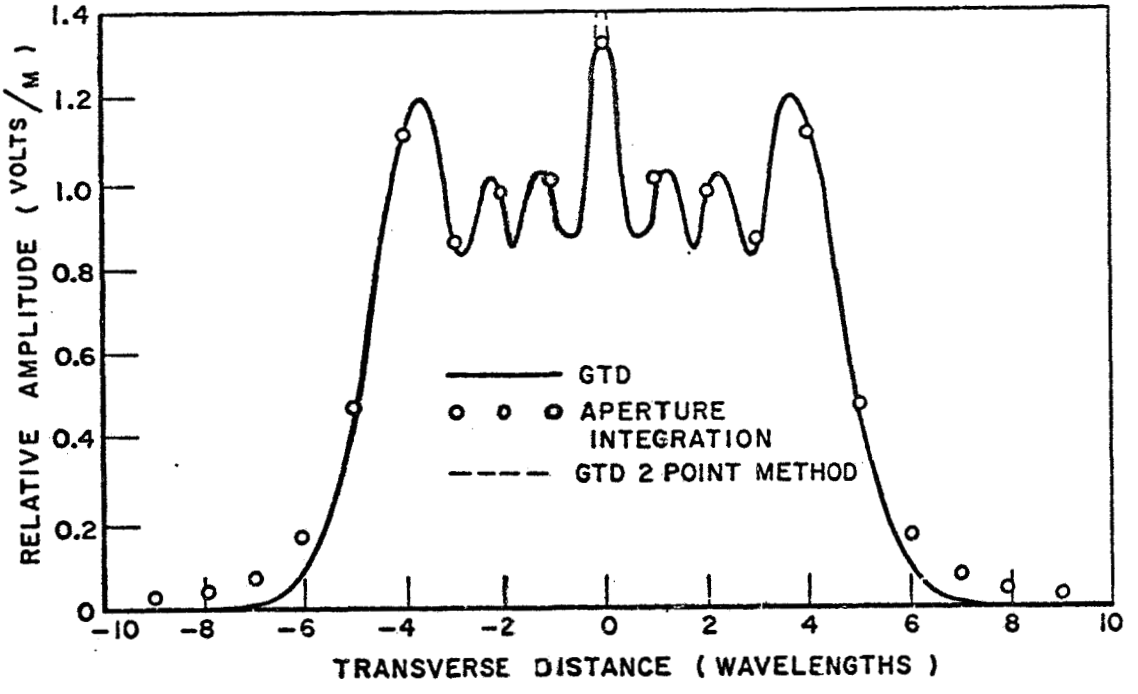

Figure 9: Electric Field on a Plane 2 Wavelengths From a Uniformly Illuminated Antenna

TABLE I

NEAR FIELD OF UNIFORM CIRCULAR ANTENNA ON A PLANE SURFACE 2 WAVELENGTHS FROM THE ANTENNA*

Transverse Distance	Geometric Theory of Diffraction		Plane Wave Spectrum	Aperture Integration
	RSB	ISB + RSB		
0.0		1.3420	1.3101	1.3356
0.5	.9290	.8912	.9186	.9170
1.0	1.0470	1.0710	1.0547	1.0640
1.5	.9732	.9612	.9679	.9670
2.0	.9993	.9986	1.0022	.9963
2.5	1.0500	1.0770	1.0566	1.0663
3.0	.8875	.8387	.8771	.8666
3.5	1.1290	1.1750	1.1379	1.1447
4.0	1.1020	1.1430	1.1066	1.1083
4.5	.8073	.8049	.8102	.8115
5.0	.4930	.4420	.4765	.4751
5.5	.2921	.2312	.2883	.2911
6.0	.1699	.1030	.1713	.1756
6.5	.1020	.0364	.1060	.1093
7.0	.0686	.0115	.0737	.0771
7.5	.0511	.0061	.0569	.0602
8.0	.0403	.0034	.0457	.0493
8.5	.0326	.0044	.0373	.0411
9.0	.0269	.0055	.0313	.0346
9.5	.0245	.0065	.0260	.0293

* Data and curves show GTD equivalent current results for the first wavelength from the axis, and two point method results for the remainder of the plane.

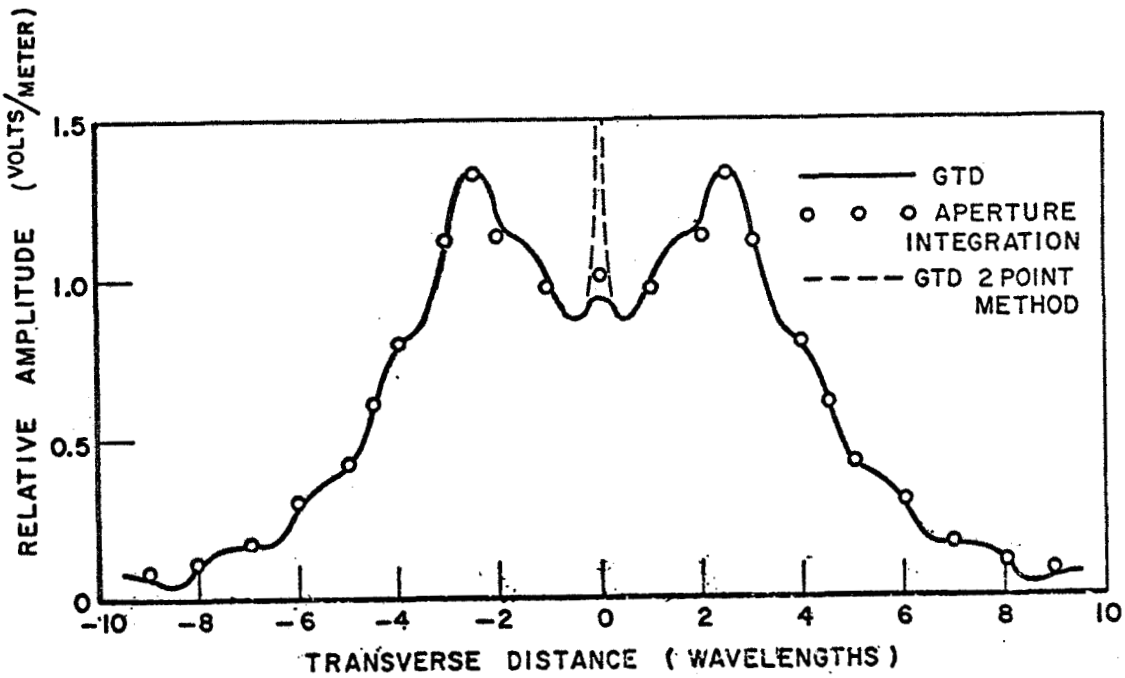

Figure 10: Electric Field on a Plane 10 Wavelengths From a Uniformly Illuminated Antenna

TABLE II

NEAR FIELD OF UNIFORM CIRCULAR ANTENNA ON A PLANE

SURFACE 10 WAVELENGTHS FROM THE ANTENNA

Transverse Distance	Geometric Theory of Diffraction		Plane Wave Spectrum	Aperture Integration
	RSB	ISB + RSB		
0.0		.9560	1.0212	1.0302
0.5	.8642	.8827	.8843	.8873
1.0	.9963	1.0090	.9815	.9837
1.5	1.0910	1.1180	1.0879	1.0902
2.0	1.1500	1.1620	1.1468	1.1470
2.5	1.2830	1.3430	1.2978	1.3032
3.0	1.1070	1.1350	1.1293	1.1308
3.5	.8655	.8556	.8817	.8780
4.0	.7853	.7963	.8008	.8011
4.5	.6207	.6093	.6138	.6145
5.0	.4611	.4242	.4244	.4234
5.5	.3995	.3843	.3836	.3860
6.0	.3151	.2964	.3050	.3063
6.5	.2044	.1658	.1954	.1931
7.0	.1785	.1527	.1770	.1773
7.5	.1714	.1549	.1733	.1763
8.0	.1261	.1023	.1259	.1283
8.5	.0829	.0481	.0811	.0812
9.0	.0830	.0601	.0845	.0850
9.5	.0893	.0726	.0927	.0946

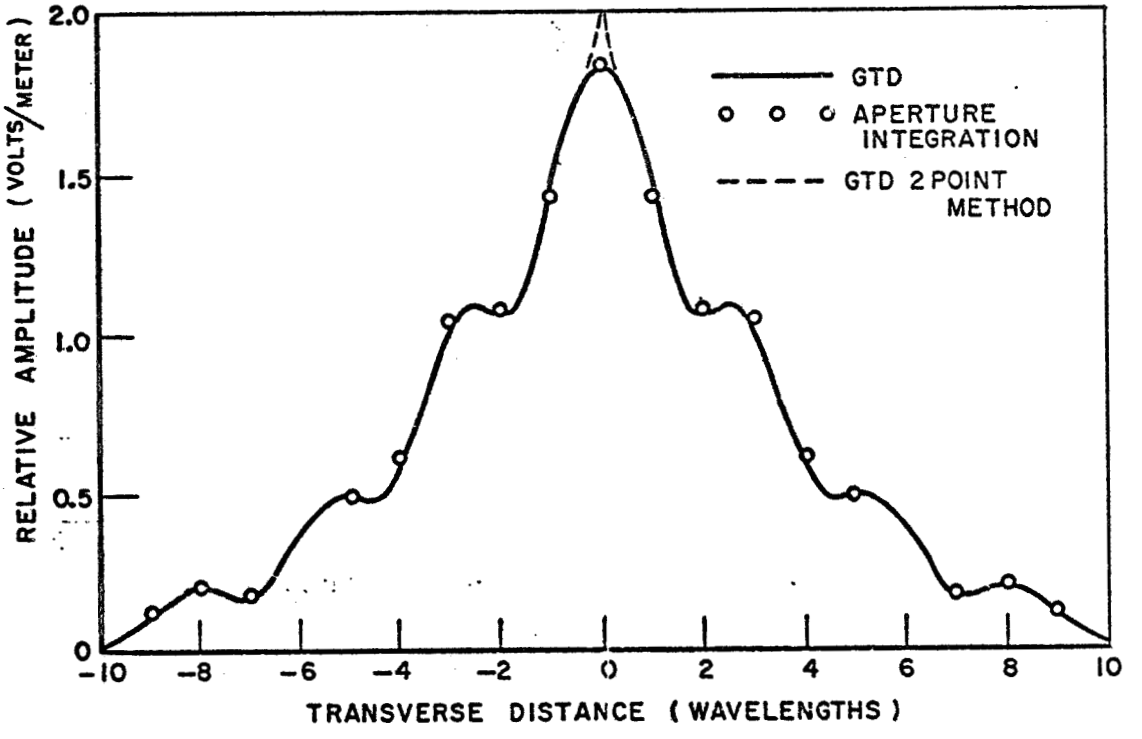

Figure 11: Electric Field on a Plane 20 Wavelengths From a Uniformly Illuminated Antenna

TABLE III

NEAR FIELD OF UNIFORM CIRCULAR ANTENNA ON A PLANE SURFACE 20 WAVELENGTHS FROM THE APERTURE

Transverse Distance	Geometric Theory of Diffraction		Plane Wave Spectrum	Aperture Integration
	RSB	ISB + RSB		
0.0		1.8500	1.8419	1.8472
0.5	1.7650	1.8770	1.7179	1.7226
1.0	1.4030	1.4550	1.4220	1.4242
1.5	1.1260	1.1310	1.1528	1.1527
2.0	1.0440	1.0510	1.0769	1.0768
2.5	1.0560	1.0840	1.0960	1.0975
3.0	.9909	1.0200	1.0282	1.0305
3.5	.8119	.8197	.8355	.8370
4.0	.6049	.5843	.6069	.6064
4.5	.4930	.4641	.4757	.4741
5.0	.4983	.4866	.4586	.4581
5.5	.4618	.4600	.4346	.4352
6.0	.3716	.3633	.3497	.3500
6.5	.2552	.2312	.2380	.2372
7.0	.1862	.1559	.1773	.1765
7.5	.1916	.1768	.1897	.1907
8.0	.1989	.1922	.1983	.2004
8.5	.1710	.1624	.1694	.1712
9.0	.1189	.1023	.1160	.1167
9.5	.0781	.0512	.0758	.0749

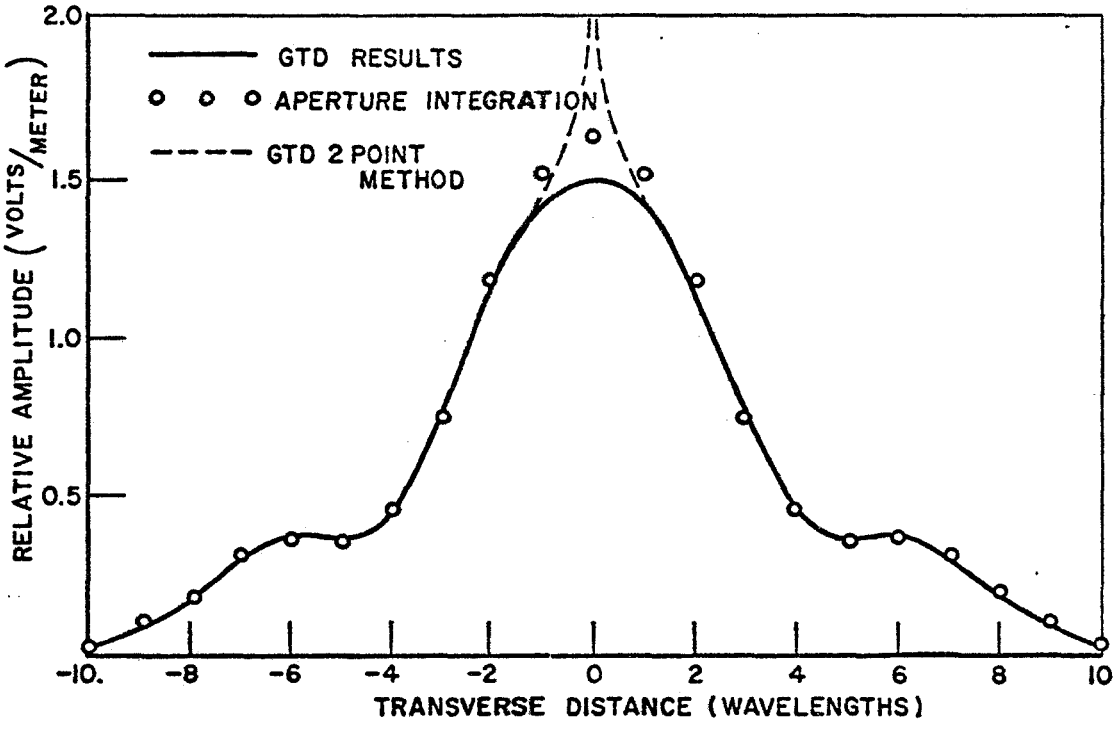

Figure 12: Electric Field on a Plane 40 Wavelengths From a Uniformly Illuminated Antenna

TABLE IV

NEAR FIELD OF A UNIFORM CIRCULAR ANTENNA ON A PLANE SURFACE 40 WAVELENGTHS FROM THE APERTURE

Transverse Distance	Geometric Theory of Diffraction		Plane Wave Spectrum	Aperture Integration
	RSB	ISB + RSB		
0.0		1.5000	1.6528	1.6536
0.5	1.6520	1.4570	1.6209	1.6224
1.0	1.4630	1.3940	1.5304	1.5315
1.5	1.3040	1.3480	1.3878	1.3891
2.0	1.1320	1.1620	1.2071	1.2080
2.5	.9502	.9651	1.0040	1.0048
3.0	.7714	.7718	.7987	.7992
3.5	.6121	.5994	.6131	.6135
4.0	.4913	.4689	.4721	.4721
4.5	.4274	.4026	.3947	.3946
5.0	.4234	.4046	.3754	.3754
5.5	.4085	.3991	.3811	.3814
6.0	.4012	.3985	.3815	.3820
6.5	.3824	.3820	.3625	.3631
7.0	.3404	.3391	.3222	.3228
7.5	.2825	.2779	.2658	.2661
8.0	.2169	.2071	.2020	.2020
8.5	.1550	.1388	.1433	.1427
9.0	.1132	.0918	.1067	.1058
9.5	.1058	.0886	.1054	.1046

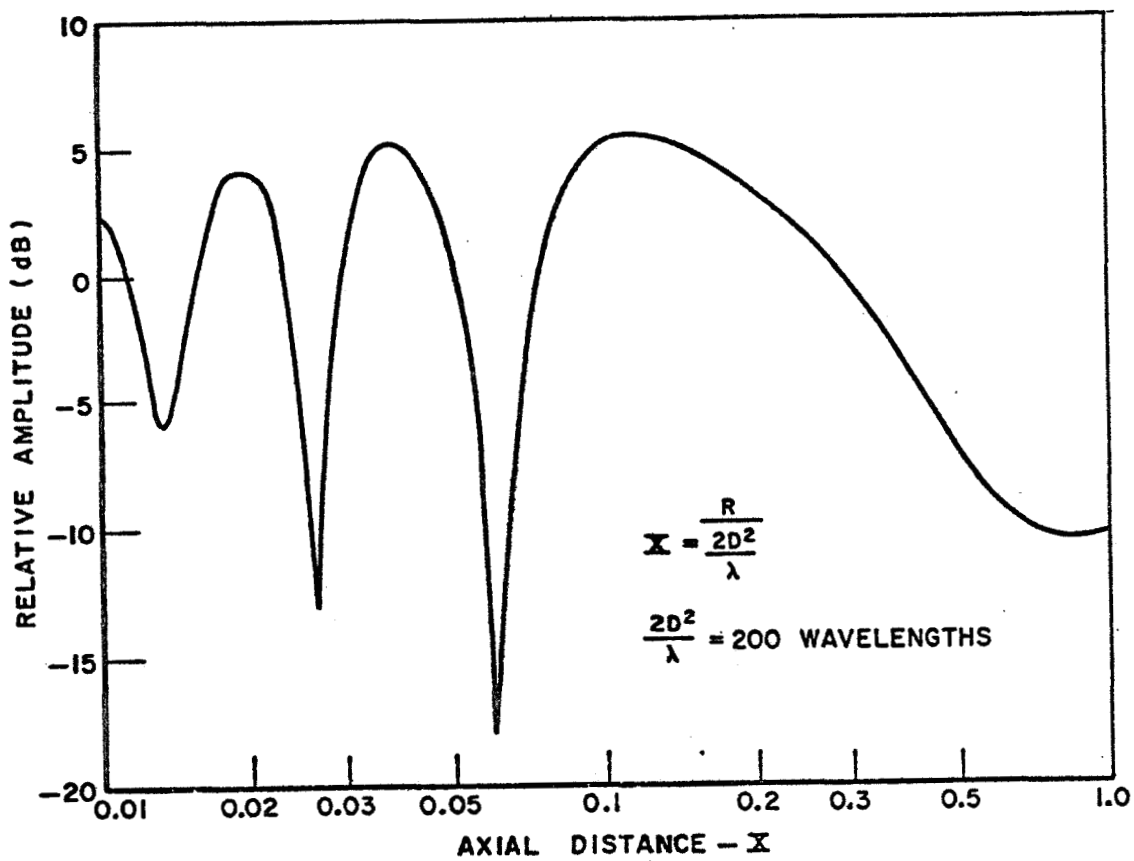

Figure 13: Electric Fields on the Axis of a Uniformly Illuminated Antenna

IV. Near Fields of an Actual Antenna

The near zone fields of an actual parabolic antenna were computed and compared with measured results. The antenna studied was a 24-inch diameter 8-inch focal length spun aluminum dish with sharp edges. The antenna was fed with a section of open ended wave guide with a plain flange. The feed was supported on a tripod constructed of 3/8-inch diameter polystyrene rods. The rods were fastened to the dish about 2 inches from the edge to reduce interaction with diffraction effects. Feed patterns are presented in Figure 14: The antenna was driven by a Sylvania Model 3200 avalanche diode oscillator mounted on the feed.

Direct current was fed to the diode oscillator through a miniature coaxial cable. The avalanche diode power source was chosen to minimize the cross section of components in the main beam of the antenna with the intent of minimizing spurious pattern disturbances due to aperture blockage. The antenna measurements were made in the Student Antenna Laboratory, Room 731 in the Electronics Laboratory. This room occupies two floors of the building providing a 20 x 20 x 40 foot volume for antenna measurements. The room surfaces are conventionally constructed with asphalt tile floor, plaster walls and a suspended grid ceiling. Eccosorb has been applied to a six-foot square area of the side walls and one end wall to reduce specular reflections. Facilities available include a pattern recorder for plotting polar antenna patterns. This

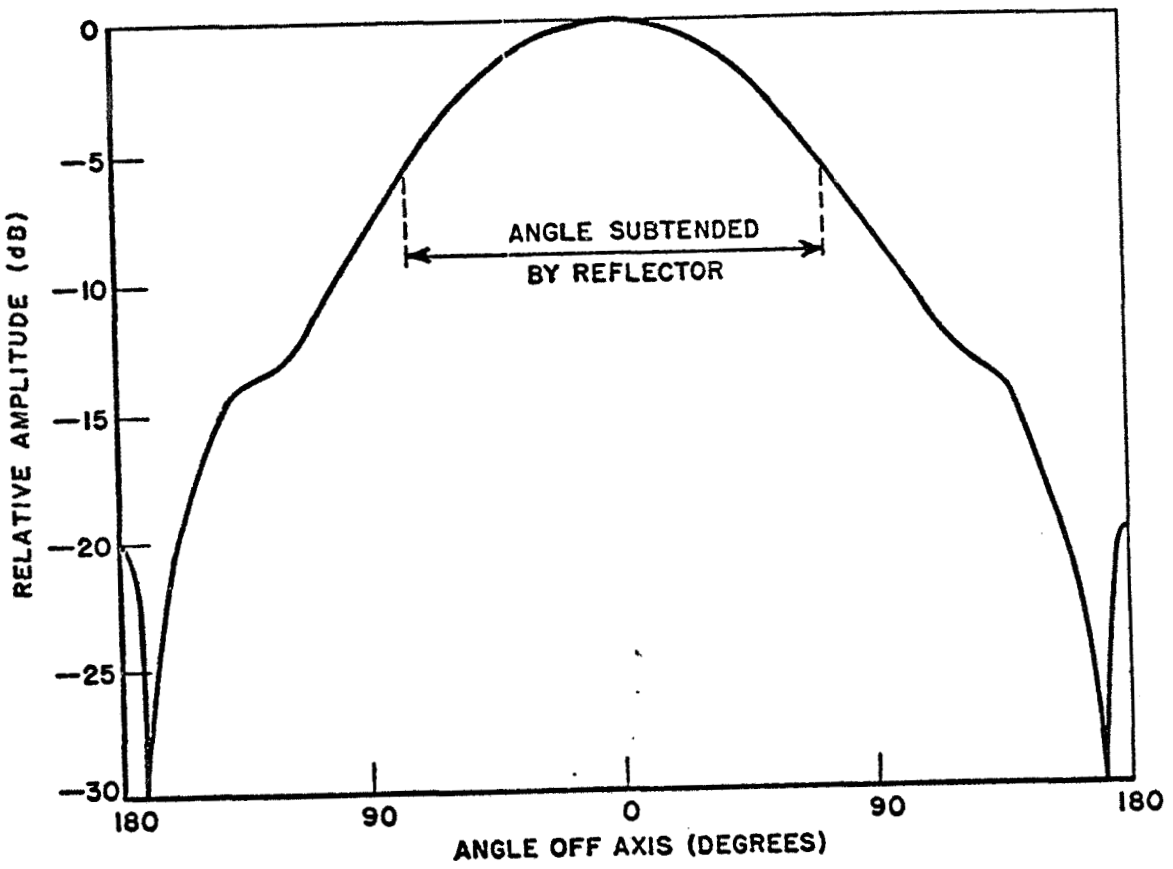

Figure 14: Open End Waveguide Feed Pattern

plotter was adapted to allow plotting straight line scans. The antenna was mounted on a 10-foot mast in the center of the room. The probe consisted of an open-ended wave guide section mounted on a moveable carriage and coupled to a crystal detector. Adequate signal level was obtained at all ranges.

The development of Section II must be modified to include the illumination taper introduced by the feed pattern. Two corrections are required, one is that the field at the reflector rim is reduced, and the second is that the geometrical optics field must vary across the aperture. The reduced value of the field at the edge can be introduced by a constant multiplicative factor in the calculations.

To find the geometrical optics field, we need to find the power density in the aperture as a function of distance from the axis. The power density gives the field in the aperture, and we can then use the principal of stationary phase to assert that the geometrical optics field can be related to the field in the aperture at the stationary point. The stationary phase arguement that follows may be used to derive (17).

The radiation integral is of the form

$$u(y,z)=\int_{-A}^{A} F(y',0)\, e^{-j\,\phi(y-y',z)}\, dy' . \qquad (64)$$

For the stationary phase principle to apply

$$\left.\frac{\partial \phi}{\partial y'}\right|_{y'=0} = 0 \,, \tag{65}$$

must be satisfied at some point y_o, called the stationary point. In our problem

$$\phi(y-y',z) = k\sqrt{(y-y')^2+z^2} \approx kz\left[1+\frac{1}{2}\left(\frac{y-y'}{z}\right)^2\right] , \tag{66}$$

where

$$kz\left(\frac{y-y'}{z}\right)^2 \geq \frac{3\pi}{2} \,, \tag{67}$$

in order that stationary phase concept be applicable,

$$\text{AND } \left(\frac{y-y'}{z}\right)^2 << 1. \tag{68}$$

This phase function fulfills (65) for $y_o = y$. The essence of the stationary phase arguement is that the limits of (64) can be reduced so that only an elemental area about y_o is considered. This is valid because the region where ϕ is slowly varying contributes more to the integral than do the regions where ϕ is varying rapidly. Once the range of integration is restricted, F(y',0) can be considered constant and taken outside the integral; and (64) becomes

$$u(y,z) = F(y,0)\, e^{-jkz} \int_{\delta} e^{-j\frac{k}{2}\left(\frac{y-y'}{z}\right)^2} dy' . \tag{69}$$

Due to the stationary process the value of the integral will not change significantly when we let the limits of integration go to infinity.

$$u(y,z) = F(y,0)\, e^{-jkz} \int_{-\infty}^{\infty} e^{-j\frac{k}{2}\left(\frac{y-y'}{z}\right)^2} dy' \tag{70}$$

The definite integral is easily evaluated. Thus we see that the field depends on the forcing function at the stationary point.

To find the aperture field, one must first find the angle ψ in Figure 15 use the far field pattern of the feed to find a reference field at each value of the angle; and then account for the ray tube spreading over the various distances from the feed to the reflector. Since the parabola collimates the diverging bundle of rays from the feed, there is no field decay in the portion of the path from the reflector to the aperture. Thus the power density in the aperture is the same as that at the reflector. The angle ψ can be simply related to the distance of the parallel ray from the axis and the focal length of the reflector.

$$\psi = 2 \arctan \frac{y}{2f}, \tag{71}$$

where y is one coordinate of the field point, and

f is the reflector focal length.

Since we know the far field pattern of the feed, one can use

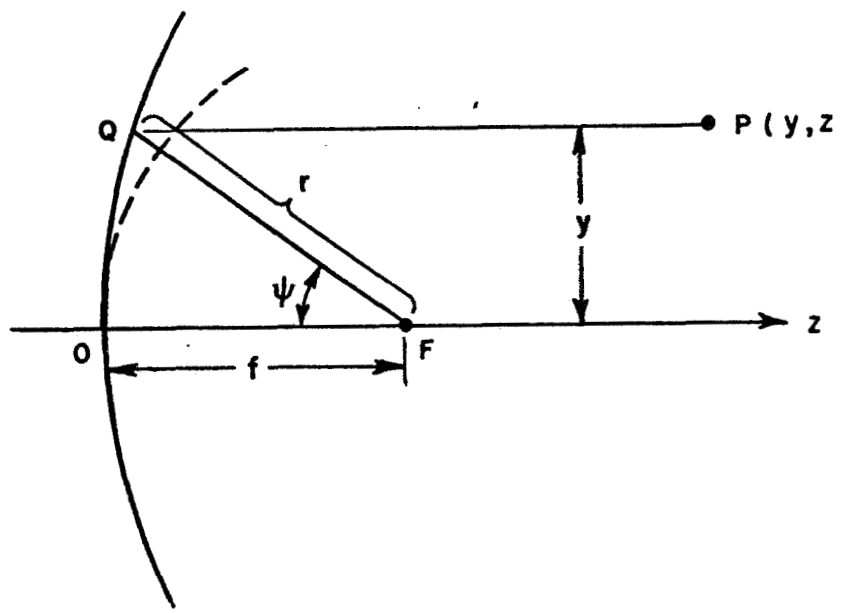

Figure 15: Geometry Used to Find Aperture Field Strength

curve fitting techniques to obtain an analytic function for the portion of the pattern illuminating the reflector. In the E-plane, this function is

$$f_e(\psi) = e^{-\left(3.95\times10^{5}\psi^2 + 1.37\times10^{-8}\psi^4\right)} . \tag{72}$$

Since f_e is unity at $\psi = 0$, it is convenient to normalize the field in terms of the field in the center of the aperture. Thus $f_e(\psi)$ represents the magnitude of the field on a spherical surface whose radius is the focal length and centered on the feed. This surface is represented by the dotted circle in Figure 15. The decay in power density as the ray travels from the surface to the reflector may be found using power conservation

$$u_r = u_s \frac{f}{r} , \tag{73}$$

where u_r is the amplitude at the reflector,

u_s is the amplitude on the surface,

f, r are shown in Figure 15.

r may be found from simple geometry to be related to the displacement of the reflected ray.

$$r = f + \frac{x^2}{4f} \tag{74}$$

These expressions may be combined to give the field in the aperture as a function of the distance of the aperture

point from the z axis.

$$E^a(y) = \frac{1}{1+\left(\frac{y}{2f}\right)^2} f_e\left(2 \arctan\left(\frac{y}{2f}\right)\right) \tag{75}$$

This expression for the geometrical optics component was summed with (35) and (48) to give the total near fields at 16.6, 37.6, 74, 117.5 and 188 wavelengths. These distances were chosen from Figure 16, a plot of the measured fields on the axis versus distance from the antenna. The distances represent maxima and minima in power density. Comparisons are shown in Figures 17 through 21.

The agreement between measured and computed results is not as good as one would have expected. Direct feed radiation and feed aperture blockage were first suspected of causing the discrepancy. The magnitude of feed radiation was estimated using geometrical optics techniques. Since the worst case radiation was of interest, it was assumed that the feed pattern was uniform at the rear axial level over the interesting portion of the rear hemisphere. Since the feed field at the center of the reflector was normalized to one, the field at any point is

$$\left|E^f(\delta)\right| = \frac{f}{\delta} f_e(\pi) = \frac{f}{10\cdot\delta}, \tag{76}$$

where δ is the distance from the feed to the field point in wavelengths.

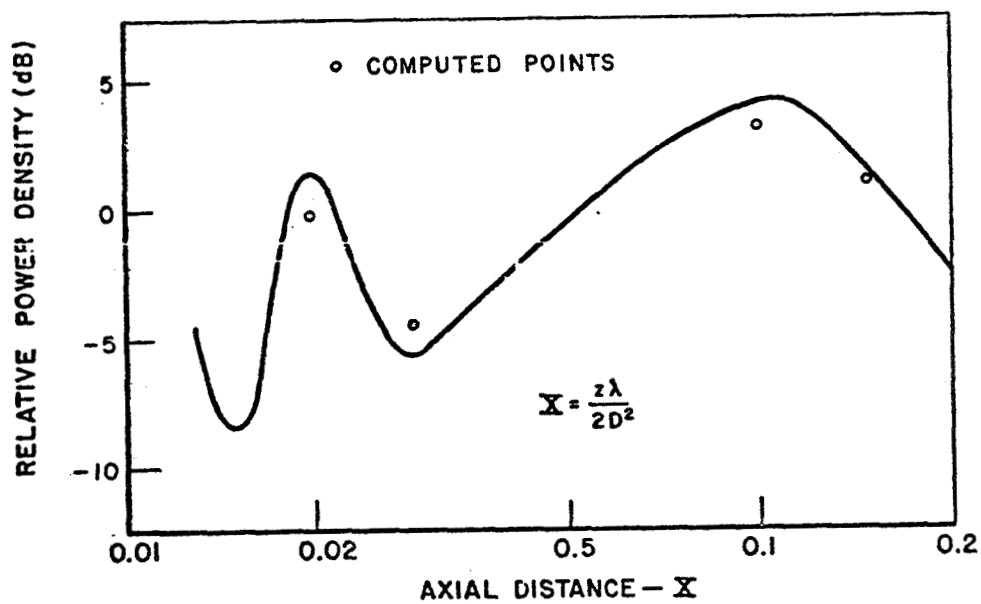

Figure 16. Measured Axial Power Density for an Antenna With Tapered Illumination, measured data in Following Figures has been Normalized to get Best Fit in the Near Zone.

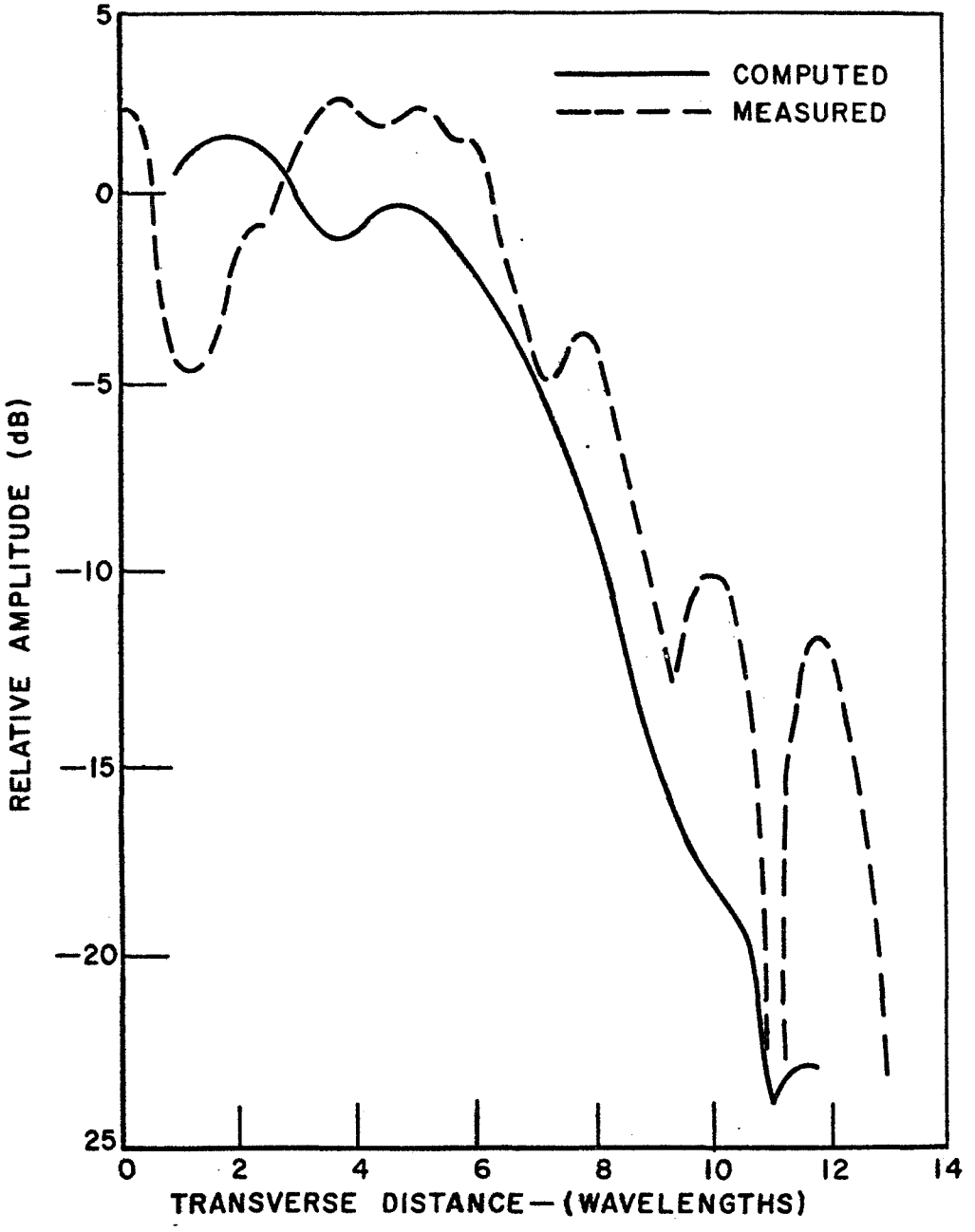

Figure 17: Electric Field on a Plane 16.6 Wavelengths From an Antenna with Tapered Illumination

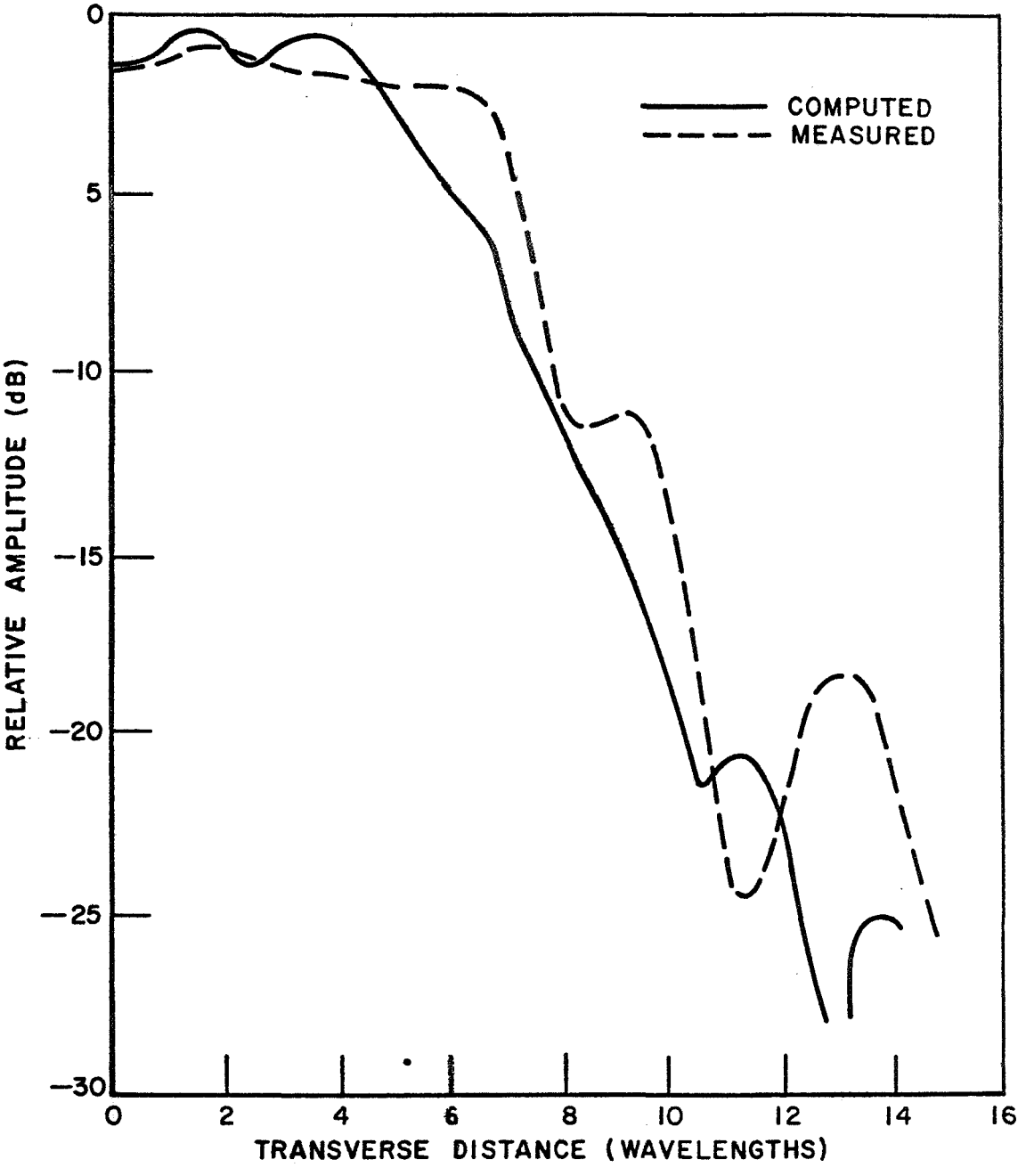

Figure 18: Electric Field on a Plane 37.6 Wavelengths From an Antenna with Tapered Illumination

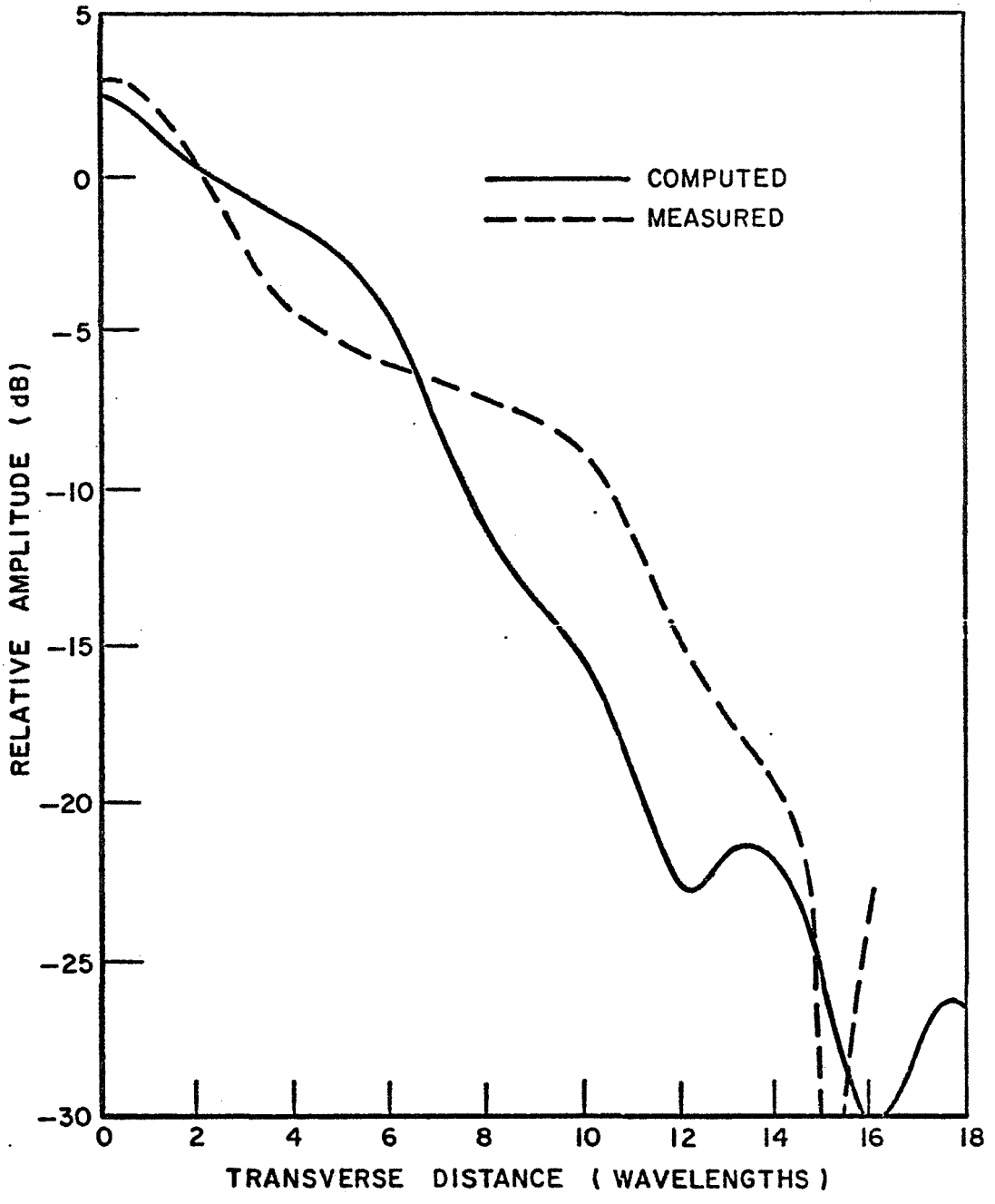

Figure 19: Electric Field on a Plane 74 Wavelengths From an Antenna with Tapered Illumination

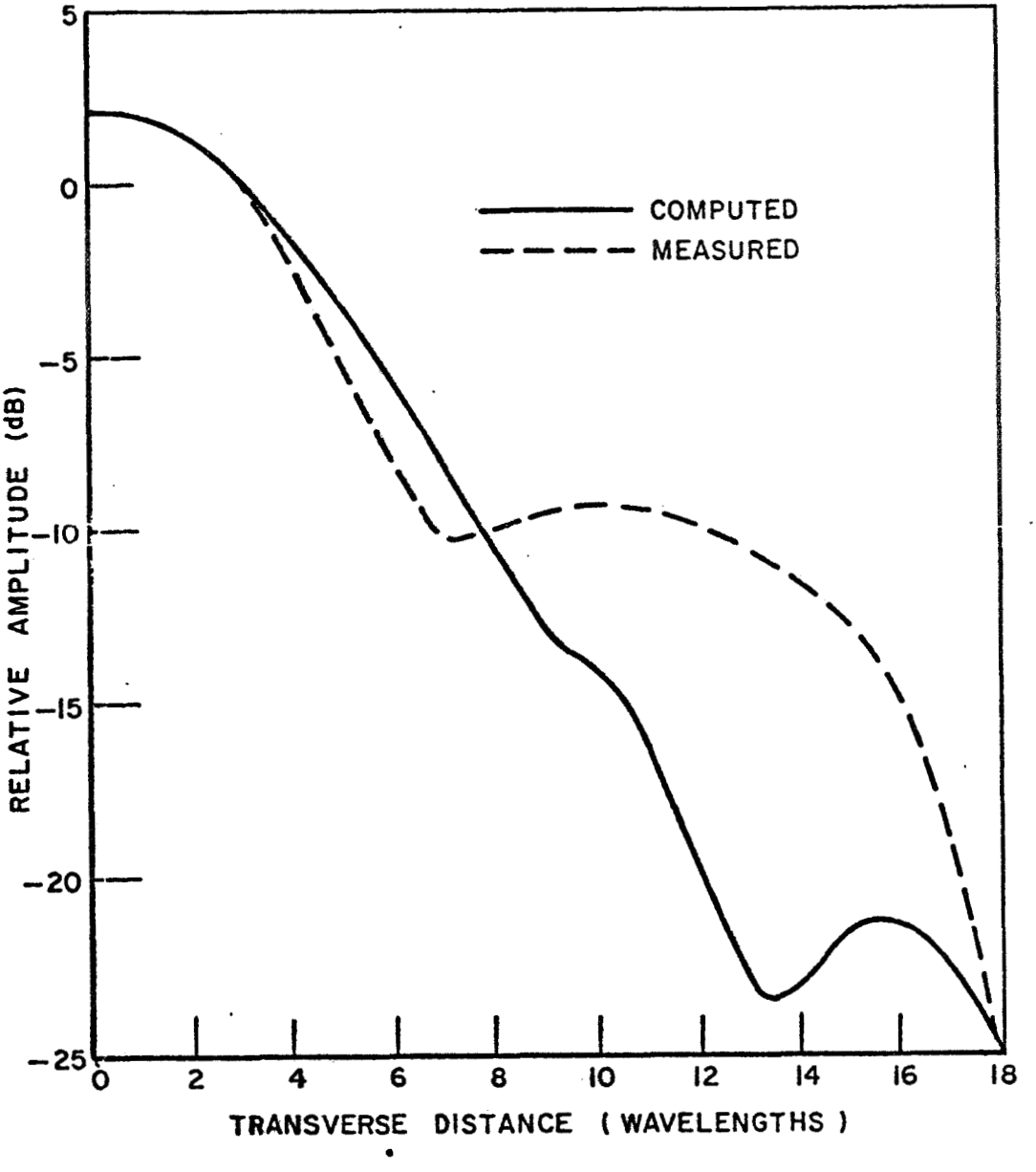

Figure 20: Electric Field on a Plane 117.5 Wavelengths From an Antenna with Tapered Illumination

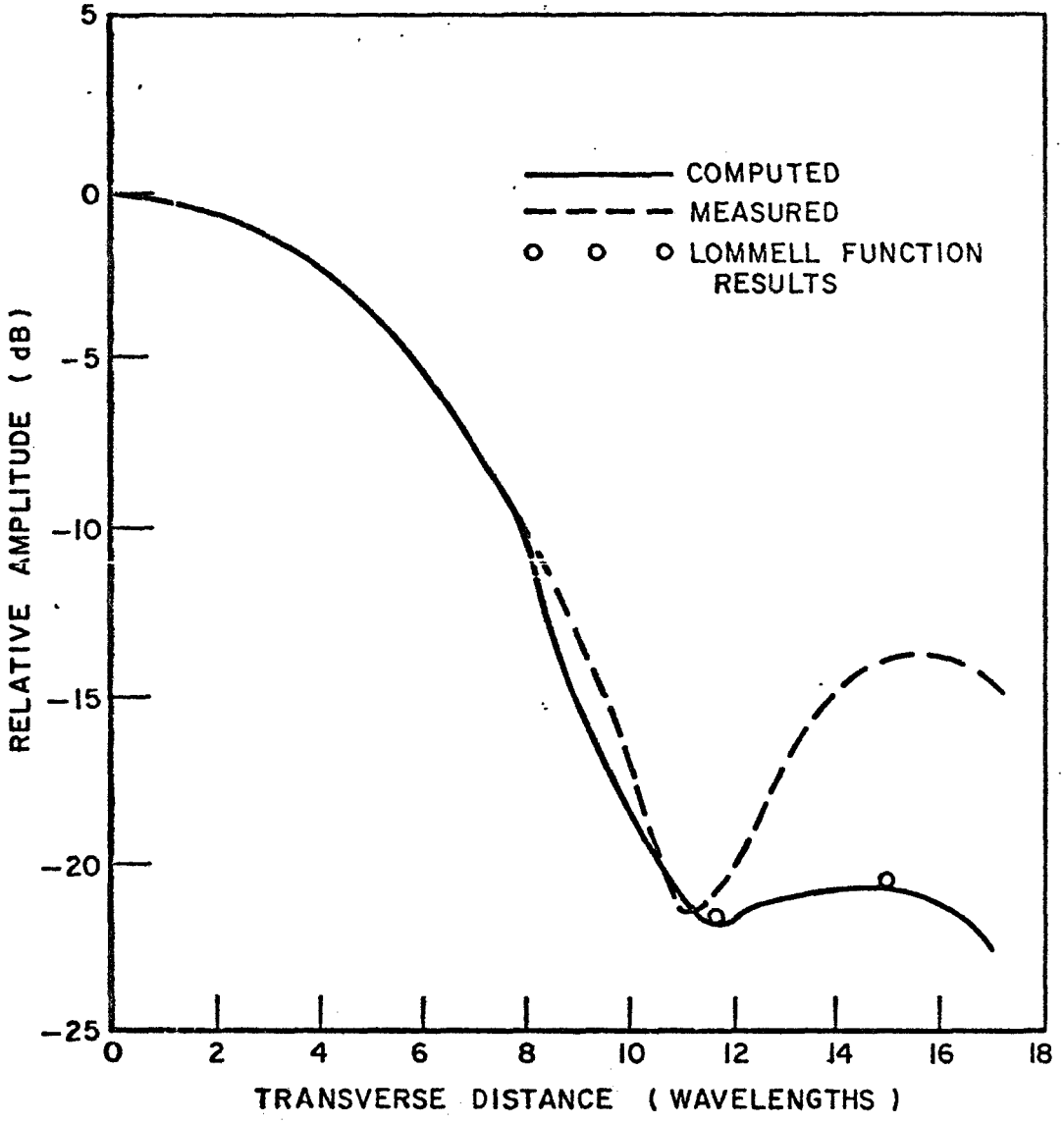

Figure 21: Electric Field on a Plane 188.0 Wavelengths From an Antenna with Tapered Illumination

For aspects close to the axis

$$\delta = z - d, \tag{77}$$

where d is the distance from the feed to the aperture.

The results of the estimation are shown in Table V.

To estimate aperture blockage, the blocking components were conceptually replaced with an equivalent source. The source is planar, equal in size to the projected size of the blocking components and driven by fields equal in magnitude but opposite in phase to the fields present in the plane of the blocking components in the absence of the blocking components. The blocking components are the metal waveguide components and the polystyrene mount. This complex assembly was modelled by a 2λ diameter disc. Since the disc is small, the far field approximation is used to find its field. Again being interested in the worst case, the scattering pattern was assumed constant at its maximum level. Use the same notation as for the feed radiation

$$\left|E^{ab}(\delta)\right| = \frac{kA^2}{2\delta} = \frac{3.14}{\delta}. \tag{78}$$

Comparing the results of the above estimates with the diffracted fields in Table V, we see that aperture blockage dominates over feed radiation near the axis. At the smaller ranges, aperture blocking is sufficiently strong to cause errors. However the discrepancy at 188λ shown in Figure 21

TABLE V

COMPARISON OF FEED, APERTURE BLOCKAGE

AND DIFFRACTION FIELDS

Distance Wavelengths	Feed Radiation	Aperture Blockage	Diffraction On Axis	Diffraction 5λ Outside SB
16.6	.045	.270	.2929	.0384
23.3	.031	.170	.3525	.0396
37.6	.018	.100	.4136	.0584
72.0	.009	.051	.4892	.0839
117.5	.005	.028	.5563	.0589
118.0	.0036	.018	.6311	.0925

cannot be explained by this mechanism. The side lobe error is especially severe.

At this point it was decided to calculate the expected pattern by a second method. The pattern at 188 λ was chosen for comparison because it is well into the Fresnel zone, and Lommel functions may be used to perform the radiation integration in closed form. The results of a hand calculation of two points on the side lobe are shown in Figure 21. This calculation was based on a uniformly illuminated aperture. The results were modified to correspond with the GTD model for the tapered aperture by reducing the uniform illumination in the Lommel calculations to the same level as the edge illumination in the GTD model. Since the GTD model does not include the effects of the illumination taper at the edge, this is a valid step. The Lommel results agree precisely with the GTD results showing that the experimental data are faulty.

The experimental method was reviewed to determine the source of the deviation. After considering room reflections and plotter errors, it became apparent through repeated study of the patterns that the 188 λ pattern was characteristic of a far field pattern. The null between the main lobe and the first side lobe was especially strange since the distance involved was about one quarter of the far field criterion. The appearance of a far field pattern in the near zone brought to mind the antenna focusing procedure. Since space was restricted

in the laboratory and the location of the test antenna was fixed to stabilize reflection, the antenna was focused with the test antenna and the probe spaced by 188λ . The feed was positioned for best gain and side lobe ratio. This results in the far field pattern appearing in the Fresnel zone. It is interesting to calculate the effect of this feed position.

Assuming that the feed position causes a phase taper in the aperture which is the best fit to a spherical wave with radius equal to the spacing between the test antenna and the probe, the maximum phase change across the aperture is given by

$$\Delta\phi = z\left(1 - \cos\frac{\theta}{2}\right), \tag{79}$$

where z is the distance between the test antenna and the probe, and

θ = 2 arc tan $\frac{A}{z}$, the angle subtended by the test antenna at the probe.

For a 19.1 λ antenna focused at 188 λ , the phase taper is 88°. The feed position for this phase error may be calculated by matching the phase shift for a central ray and an edge ray with the required error. To match an 88° phase shift, the feed must be displaced from the focal point of the reflector by .3 λ or very nearly one centimeter. To check this result, use the thin lens equation

$$\frac{1}{f} = \frac{1}{i} + \frac{1}{o} , \tag{80}$$

where i is the image (probe) distance, and

O is the object (feed) distance.

Using this relation, the required displacement of the feed is 0.22λ which agrees well with the results of phase taper matching.

Thus, this antenna adjusted for best pattern at 188 exhibits sufficient phase taper to give strong disagreement between measured results and computed results which assume no phase taper. This phase taper affects the patterns at all distances and is considered to be the mechanism that causes the disagreement between the computed and measured data.

V. Conclusions

The geometrical theory of diffraction is an effective method of calculating the near fields of reflector antennas. This work extends the results of others to treat the forward axial region by including the reflected field of the antenna beam. The methods developed in this paper fail as the field point moves into the far zone. This is not a major problem because other geometrical theory of diffraction techniques are available there.

Comparison of the results for a uniformly illuminated antenna with data obtained by aperture integration and the plane wave spectrum technique show that equivalent results are obtainable with an expenditure of much less computer time. These results prove that the geometrical theory of diffraction

is applicable in the near zone of reflector antennas.

Since the phase characteristic of the antenna used to gather experimental data did not match the model used in the computation, the results for an antenna with tapered illumination cannot be completely verified. The technique for computing fields for a tapered aperture should be improved using the traveling wave concepts used in the GTD analysis of the H-plane pattern of an open-ended rectangular wave guide. The experiment should be repeated using an antenna focused in the far field.

ACKNOWLEDGMENT

The author is indebted to Dr. Leon Peters, Jr. for suggesting the topic for this work. His continued guidance and encouragement was invaluable. The assistance of Dr. R. G. Kouyoumjian in answering many questions and suggesting alternative approaches to the feed blocking problem is appreciated. The consideration of Dr. D. Hodge in allowing the author to use the Student Antenna Laboratory and providing advice for the measurement portion of the work is appreciated. The support of the Civilian Institution Division of The Air Force Institute of Technology is recognized.

The material contained in this report is also used as a thesis submitted to the Department of Electrical Engineering, The Ohio State University as partial fulfillment for the degree Master of Science.

REFERENCES

1. Clark, D. E., Rudduck, R. C., and Wu, D. C. F., "Two Dimensional Radome Analysis by a Surface Integration Technique," The Ohio State University, ElectroScience Laboratory, Report 2767-5, 26 February 1970, prepared under Contract N000019-69-C-0325, Naval Air Systems Command.

2. Lysher, L. J., "A Study of the Near Field Behind a Parabolic Antenna," M.S. Thesis, The Ohio State University, Columbus, Ohio, 1962.

3. Peters, L., Jr. and Kilcoyne, T. E., "Radiation Mechanisms in a Reflector Antenna System," IEEE Transactions, Vol. EMC-7, pp. 368-374.

4. Ratnasiri, P. A. J., Kouyoumjian, R. G., and Pathak, P. H., "The Wide Angle Side Lobes of Reflector Antennas," The Ohio State University, ElectroScience Laboratory, Report 2183-1, 23 March 1970, prepared under Contract AF 19(628)-5929, Air Force Cambridge Research Laboratories.

5. Sommerfeld, A., Optics, New York: Academic Press, 1964, pp. 245-265.

6. Pathak, P. H., and Kouyoumjian, R. J., "The Dyadic Diffraction Coefficient For a Perfectly Conducting Wedge," The Ohio State University, ElectroScience

Laboratory, Report 2183-4, 5 June 1970, prepared under Contract AF 19(628)-5929, Air Force Cambridge Research Laboratories.

7. Kouyoumjian, R. G., unpublished notes, also given in 6.

8. Keller, H. B., "Diffraction by an Aperture," Journal of Applied Physics, Vol. 28, No. 6, pp. 426-444 (1957).

9. Richmond, Jack, unpublished notes.

10. Wu, D. C. F., "Electromagnetic Analysis of Three-Dimensional Antenna-Radomes Using the Plane Wave Spectrum - Surface Integration Technique," Ph. D. Dissertation, The Ohio State University, 1971.

11. Walter, C. H., Traveling Wave Antennas, New York: McGraw-Hill, 1965, pp. 58-62.

DISTRIBUTION LIST

	No. Copies
NASA Langley Research Center Hampton, VA 23365	
Attention: Program Reports and Analysis Unit, Mail Stop 122	1
Raymond L. Zavasky, Mail Stop 110	1
Marion C. Bailey, Mail Stop 490	1
Dr. J. S. Chatterjee, Mail Stop 490	1
J. Earl Jones, Mail Stop 490	1
Dr. John Painter, Mail Stop 490	1
Dr. Calvin T. Swift, Mail Stop 490	1
William Croswell, Mail Stop 490	5
NASA Ames Research Center Moffett Field, CA 94035	
Attention: Library, Mail Stop 202-3	1
NASA Flight Research Center P.O. Box 273 Edwards, CA 93523	
Attention: Library	1
Jet Propulsion Laboratory 4800 Oak Grove Drive Pasadena, CA 91103	
Attention: Library, Mail Stop 111-113	1
NASA Manned Spacecraft Center 2101 Webster Seabrook Road Houston, TX 77058	
Attention: Library, Code BM6	1
NASA Marshall Space Flight Center Huntsville, AL 35812	
Attention: Library	1
NASA Wallops Station Wallops Island, VA 23337	
Attention: Library	1
NASA Lewis Research Center 21000 Brookpark Road Cleveland, OH 44135	
Attention: Library, Mail Stop 60-3	1
NASA Goddard Space Flight Center Greenbelt, MD 20771	
Attention: Library	1

NASA John F. Kennedy Space Center Kennedy Space Center, FL 32899 Attention: Library, Code IS-DOC-12L	1
National Aeronautics and Space Administration Washington, DC 20546 Attention: Library, Code KSS-10 NASA Code SR	 1 1
NASA Scientific and Technical Information Facility P.O. Box 33 College Park, MD 20740	6 plus reproducible
Naval Research Laboratory 4555 Over Look Avenue, S.W. Washington, D.C. 20390 Attention: Dr. John L. Allen, Code 5000 Dr. T.L. ap Rhys, Code 5360	 1 1
Stanford Research Institute Electromagnetic Sciences Laboratories 333 Ravenswood Avenue Menlo Park, CA 94025 Attention: Dr. G. August Dr. Tetsu	 1 1
General Microwave Corporation 155 Marine Street Farmingdale, NY 11735 Attention: M. A. Balfour	 1
Environmental Sciences Services Administration/ITS Boulder, CO 80302 Attention: H. V. Cottony Dr. Mark T. Ma	 1 1
Hughes Aircraft Company 1800 W. Malvern Fullerton, CA 92634 Attention: Dr. Edward C. Dufort Dr. R. F. Hyneman Dr. At. T. Villeneuve	 1 1 1
Lockheed Missiles and Space Company Sunnyvale, CA 94088 Attention: John B. Damonte	 1
Lincoln Laboratory Lexington, MA 02173 Attention: Bliss L. Diamond, Mail Stop 35 Dr. Leon J. Ricardi Dr. John Ruze	 1 1 1

Wheeler Laboratory, Inc.
P.O. Box 561
Smithtown, NY 11787
Attention: Peter W. Hannan 1
H. W. Redlien, Jr. 1

Andrew Corporation
Head Antenna Design
10500 W. 153rd. Street
Orland Park, IL 60642
Attention: Larry Hauseu 1
Dr. C. M. Knop 1

Air Force Cambridge Research Laboratories
L. G. Hanscom Field
Bedford, MA 01730
Attention: Dr. F. S. Holt (CRDG) 1
Dr. R. J. Mallioux 1
Dr. Richard B. Mack (CRDG) 1
Dr. John Schindler (CRDG) 1
Walter Rotman 1

Jet Propulsion Laboratory
Antenna Propagation Group
4800 Oak Grove Drive
Pasadena, CA 91103
Attention: Dr. Arthur C. Ludwig, Mail 238-808 1

IIT Research Institute
10 West 35th Street
Chicago, IL 60616
Attention: Dr. Alan W. Radge 1

Sperry Rand Research Center
Sudbury, MA 01776
Attention: Dr. Gerald Ross 1

Flights Aircraft Company
Microwave Department
Box 3310
Fullerton, CA 92634
Attention: Dr. Louis Stank 1

Bell Telephone Laboratories
Whippany, NJ 07981
Attention: Dr. C. P. Wu 1

TRF, Inc.
400 Border Street
East Boston, MA 02128
Attention: Dr. Alan J. Simmons 1

Radio Corporation of America
Advanced Microwave Technology
Missile and Surface Radar Division
Defense Electronics Products
Moorestown, NJ 08057
Attention: Dr. Willard T. Patton 1

The Ohio State University
Department of Electrical Engineering
2024 Neil Avenue
Columbus, OH 43210
Attention: Dr. W. D. Burnside 1
Dr. R. T. Compton 1
Dr. Robert G. Kouyoumjian 1
Dr. H. C. Ko 1
Dr. C. A. Levis 1
Dr. B. A. Munk 1
Dr. P. Pathak 1
Dr. Roger C. Rudduck 1

The Ohio State University
ElectroScience Laboratory
1320 Kinnear Road
Columbus, OH 43212
Attention: Dr. E. M. Kennaugh 1
Dr. A. A. Ksienski 1
Dr. C. H. Walter 1
Dr. Jack H. Richmond 1

West Virginia University
Department of Electrical Engineering
Morgantown, West Virginia 26506
Attention: Dr. C. A. Balanis 1

Syracuse University
Syracuse, NY 13210
Attention: Dr. David K. Cheng 1

Syracuse University
Department of Electrical Engineering
Syracuse, NY 13210
Attention: Dr. Roger F. Harrington 1
Dr. Ming-Kuei Hu 1
Dr. Bradley J. Strait 1

Polytechnic Institute
Department of Electrophysics of Brooklyn
Farmingdale, NY 11735
Attention: Dr. L. B. Eslsen 1
Dr. Alexander Hessel 1
Dr. George H. Knittel 1

University of Illinois
Department of Electrical Engineering
Urbana, IL 61803
Attention: Dr. G. A. Deschamps 1
Dr. Y. F. Lo 1
Dr. R. Mittra 1
Paul E. Mayes 1

The University of Michigan
The Radiation Laboratory
2216 Space Research Building
2455 Hayward Month Campers
Ann Arbor, MI 48105
Attention: Ralph E. Hiatt 1
Dr. Eugene F. Knott 1
Dr. C. T. Tai 1

University of California
Department of Electrical Engineering
Berkley, CA 94720
Attention: Dr. Kenneth K. Mei 1

Georgia Institute of Technology
Department of Electrical Engineering
Atlanta, GA 30332
Attention: Dr. D.T. Paris 1

North Caroline University
Department of Electrical Engineering
Raleigh, NC 27607
Attention: Dr. D. R. Rhodes 1

University of California
Applied Electrophysics Department
San Diego
LaJolla, CA 92037
Attention: Dr. V. H. Rumsey 1

George Washington University
Department of Electrical Engineering and Computer Sciences
Washington, DC 20006
Attention: Dr. Walter K. Kahn 1

Virginia Polytechnic Institute and State University
Department of Electrical Engineering
Blacksburg, VA 24060
Attention: Dr. W. L. Stutzman 1

University of Mississippi
Department of Electrical Engineering
Oxford, MS 38655
Attention: Dr. L. Tsai 1

University of Toronto
Department of Electrical Engineering
Toronto, 5
Ontario, Canada
Attention: Dr. J. L. Yen 1

Dr. William F. Gabriel
4025 Honey Lane
Annandale, VA 22003 1

Dr. R. C. Hansen
18651 Wells Drive
Tarzana, CA 91356 1

Dr. E. M. T. Jones (TCI)
1623 Stierlin Road
Mountain View, CA 94040 1

John P. Shelton
1701 N. Ft. Myer Drive
Arlington, VA 22209 1

Dr. R. L. Tanner
1625 Stierlin Road
Mountain View, CA 94040 1